

PAPER • OPEN ACCESS

Raman spectroscopy in layered hybrid organic-inorganic metal halide perovskites

To cite this article: Davide Spirito *et al* 2022 *J. Phys. Mater.* **5** 034004

View the [article online](#) for updates and enhancements.

You may also like

- [Temperature-dependent optical properties of hybrid organic-inorganic perovskite single crystals \(\$\text{CH}_3\text{NH}_3\text{PbI}_3\$ and \$\text{CH}_3\text{NH}_3\text{PbBr}_3\$ \)](#)
Sangheon Park, Yu-Seong Seo, Chang Won Ahn *et al.*
- [Recent progress of the optoelectronic properties of 2D Ruddlesden-Popper perovskites](#)
Haizhen Wang, Chen Fang, Hongmei Luo *et al.*
- [Perovskite-inspired materials for photovoltaics and beyond—from design to devices](#)
Yi-Teng Huang, Seán R Kavanagh, David O Scanlon *et al.*



ECS Membership = Connection

ECS membership connects you to the electrochemical community:

- Facilitate your research and discovery through ECS meetings which convene scientists from around the world;
- Access professional support through your lifetime career;
- Open up mentorship opportunities across the stages of your career;
- Build relationships that nurture partnership, teamwork—and success!

Join ECS!

Visit electrochem.org/join





PAPER

OPEN ACCESS





RECEIVED
19 April 2022REVISED
29 May 2022ACCEPTED FOR PUBLICATION
16 June 2022PUBLISHED
5 July 2022

Original content from this work may be used under the terms of the [Creative Commons Attribution 4.0 licence](https://creativecommons.org/licenses/by/4.0/).

Any further distribution of this work must maintain attribution to the author(s) and the title of the work, journal citation and DOI.



Raman spectroscopy in layered hybrid organic-inorganic metal halide perovskites

Davide Spirito^{1,*} , Yaiza Asensio² , Luis E Hueso^{3,3}  and Beatriz Martín-García^{2,*} ¹ IHP–Leibniz-Institut für innovative Mikroelektronik, Im Technologiepark 25, 15236 Frankfurt (Oder), Germany² CIC nanoGUNE BRTA, Tolosa Hiribidea, 76, 20018 Donostia-San Sebastián, Basque Country, Spain³ IKERBASQUE, Basque Foundation for Science, Bilbao, Basque Country, 48009, Spain

* Authors to whom any correspondence should be addressed.

E-mail: spirito@ihp-microelectronics.com and b.martingarcia@nanogune.eu**Keywords:** hybrid organic-inorganic metal halide perovskites, layered materials, Raman spectroscopy, phase transition, phonon

Abstract

The continuous progress in the synthesis and characterization of materials in the vast family of hybrid organic-inorganic metal halide perovskites (HOIPs) has been pushed by their exceptional properties mainly in optoelectronic applications. These works highlight the peculiar role of lattice vibrations, which strongly interact with electrons, resulting in coupled states affecting the optical properties. Among these materials, layered (2D) HOIPs have emerged as a promising material platform to address some issues of their three-dimensional counterparts, such as ambient stability and ion migration. Layered HOIPs consist of inorganic layers made of metal halide octahedra separated by layers composed of organic cations. They have attracted much interest not only for applications, but also for their rich phenomenology due to their crystal structure tunability. Here, we give an overview of the main experimental findings achieved via Raman spectroscopy in several configurations and set-ups, and how they contribute to shedding light on the complex structural nature of these fascinating materials. We focus on how the phonon spectrum comes from the interplay of several factors. First, the inorganic and organic parts, whose motions are coupled, contribute with their typical modes which are very different in energy. Nonetheless, the interaction between them is relevant, as it results in low-symmetry crystal structures. Then, the role of external stimuli, such as temperature and pressure, which induce phase transitions affecting the spectrum through change in symmetry of the lattice, octahedral tilting and arrangement of the molecules. Finally, the relevant role of the coupling between the charge carriers and optical phonons is highlighted.

1. Introduction

Hybrid organic-inorganic metal halide perovskites (HOIPs) arrived in 2009 as promising materials for photovoltaics with a power conversion efficiency of 3.8% [1], which nowadays exceeds 25% [2]. These materials with already demonstrated extraordinary optoelectronic performance in photovoltaics [3, 4], LEDs [5] and photodetectors [6], surpass organic electronics in terms of their figures-of-merit and reach values close to or above Si and semiconductor technology, due to their high optical absorption coefficient, tuneable band-gap, near-unity photoluminescence (PL) quantum yield, low trap densities and excellent excitonic and charge carrier mobility, in addition to their low-cost processability and tuneable crystal structure and composition [3, 4, 7–15]. Nevertheless, continuous efforts are being made to address several challenges originating from the composition and mixed ionic-electronic conductivity of HOIPs for their successful application in optoelectronic devices, such as the presence of Pb [16, 17], low ambient stability (thermal stress, light or oxygen/moisture) [15, 18–20], or ion migration under operation [10, 18, 21–23]. The development of environmentally friendly Pb-free candidates [10, 24–28] aiming at replacing the toxic Pb [18] led to the appearance of double HOIPs, which also present better ambient stability. These double HOIPs emerge from the three-dimensional (3D) HOIPs, with general formula $A^I B^{II} X_3$ (A = small organic or

inorganic alkaline cation; B = metal cation and X = halide anion), where B = Pb^{2+} , can be replaced by a combination of trivalent (Bi^{3+} , Sb^{3+}) and monovalent (Ag^+ , Cu^+ , Au^+ , K^+) cations [18, 29–34]. Moreover, the dimensional reduction of the 3D HOIPs by introducing large-size cations in the A-site of the crystal structure allows accessing the layered (2D) counterparts. Since both materials, 3D and 2D, share the same inorganic part, their properties and applications are closely related, but the tunability of the crystal structure of the 2D HOIPs makes them a more rich and flexible material platform [13, 30, 35–38]. Compared to 3D HOIPs, layered HOIPs offer an enhanced ambient stability together with a more versatile crystal structure and dimensionality, which facilitates their incorporation in miniaturized and flexible electronic devices and creates new opportunities for tailor-made materials. The physicochemical properties of layered HOIPs can be tuned by varying the number of octahedral layers (dimensionality, denoted as n), the metal cation, the halogen anion and the large organic cation [13, 35–37]. Additionally, since 2D HOIPs consist of anionic metal halide sheets separated by organic cation layers, this enables their mechanical exfoliation, similarly to graphene-related materials [39]. They have already demonstrated to be good candidates for optoelectronic applications [3, 40] in particular, 2D/3D solar cells [3, 18], LEDs [41] and photodetectors [42].

Further development of layered HOIPs and the materials selection require exploring the crystal structure and lattice dynamics and their effect on optical and electronic properties. For this purpose, Raman spectroscopy has shown to be a non-destructive, accessible, and sensitive technique for monitoring simultaneously the structural changes related to the rearrangement of the inorganic cage and A-site cations. Indeed, in the case of 3D HOIPs, Raman spectroscopy has been used to determine phase transition origin and temperature onset [11, 43–46], to probe local strain [9, 47], and to check the material's degradation [48–51], composition [11, 52–54], and quality in terms of crystallinity and polymorphs [44, 55, 56]. In this review, we focus our attention on the vibrational properties of 2D HOIPs and how Raman spectroscopy can help to disentangle the complexity of these materials. We aim to offer a comprehensive assessment of the research progress made with these materials, which is still in an early stage compared to their 3D counterparts. Therefore, we will discuss the relevance of using Raman spectroscopy to study the inorganic and organic Raman modes of 2D HOIPs and their interactions, their phase transitions and their phonon interactions.

2. Raman scattering and experimental setups

The technical advances in optics and electronics have greatly improved the availability of Raman spectroscopy, which has become a widespread and easy to use technique in the past decades. Its great advantage is the use of UV-visible-NIR light for the investigation of very low-energy excitations in materials, occurring in the MIR-FIR range. A typical setup is shown in figure 1(a).

Raman scattering is an inelastic light scattering effect where an incident photon can lose (or gain) energy by interacting with excitations in a material. Typically, Raman spectroscopy involves interaction with phonons, i.e. quantized vibrations of solid lattices or molecules. The monochromatic excitation light interacts with the electrons in the material, and the vibrations modulate the polarizability, producing the inelastic scattering [57]. In the scattered light, the phonon modes will appear as peaks at a distinct wavelength from the excitation. Usually, the spectra are reported in terms of 'Raman shift', i.e. the energy separation from the excitation light, in units of inverse cm (cm^{-1}). The experimental set-up needs notch or bandpass filters to suppress the elastically scattered light, with the requirement of sharp edges for the blocked region. Recent technical advances in the field allow measurements at ultralow Raman shift ($<10 \text{ cm}^{-1}$). These systems (figure 1(b)) use two or three volume Bragg gratings, which act as spectral and angular filters, suppressing the elastic (Rayleigh) peak [58, 59].

Raman scattering intensity is controlled by selection rules for the polarization state of incident and scattered light. These rules are a consequence of the symmetry of the crystal or molecule. The atomic arrangement in molecules is controlled by the directionality of chemical bonds, resulting in well-defined symmetries; the symmetry operations that leave the molecule unchanged form a 'point group'. Similarly, in crystalline solids the atoms (ions) occupy well-defined positions in a periodic lattice, which therefore has an associated translational symmetry. To each crystal structure, a space group is assigned; in 3 dimensions, 230 distinct space groups exist. The space groups are classified into 32 crystal classes, according to their associated point group (i.e. the symmetry operations without translations). For layered perovskites, these point groups typically include 2- and 4-fold rotations and mirror planes (e.g. point groups D_{4h} , C_{4h} , C_{2h}). The perfect octahedron, the fundamental element of the inorganic part, is much more symmetric (group O_h), with 2-, 3-, 4-fold axes. The crystal classes can be classified into seven crystal systems. Typical systems for layered perovskites are tetragonal, orthorhombic, triclinic and monoclinic, while 3D perovskites are typically cubic at room temperature [37, 46, 60, 61].

Once the lattice and symmetry are known, the phonon modes (vibrational normal modes) can be calculated by solving the relevant dynamic equation, yielding the phononic spectrum as a function of

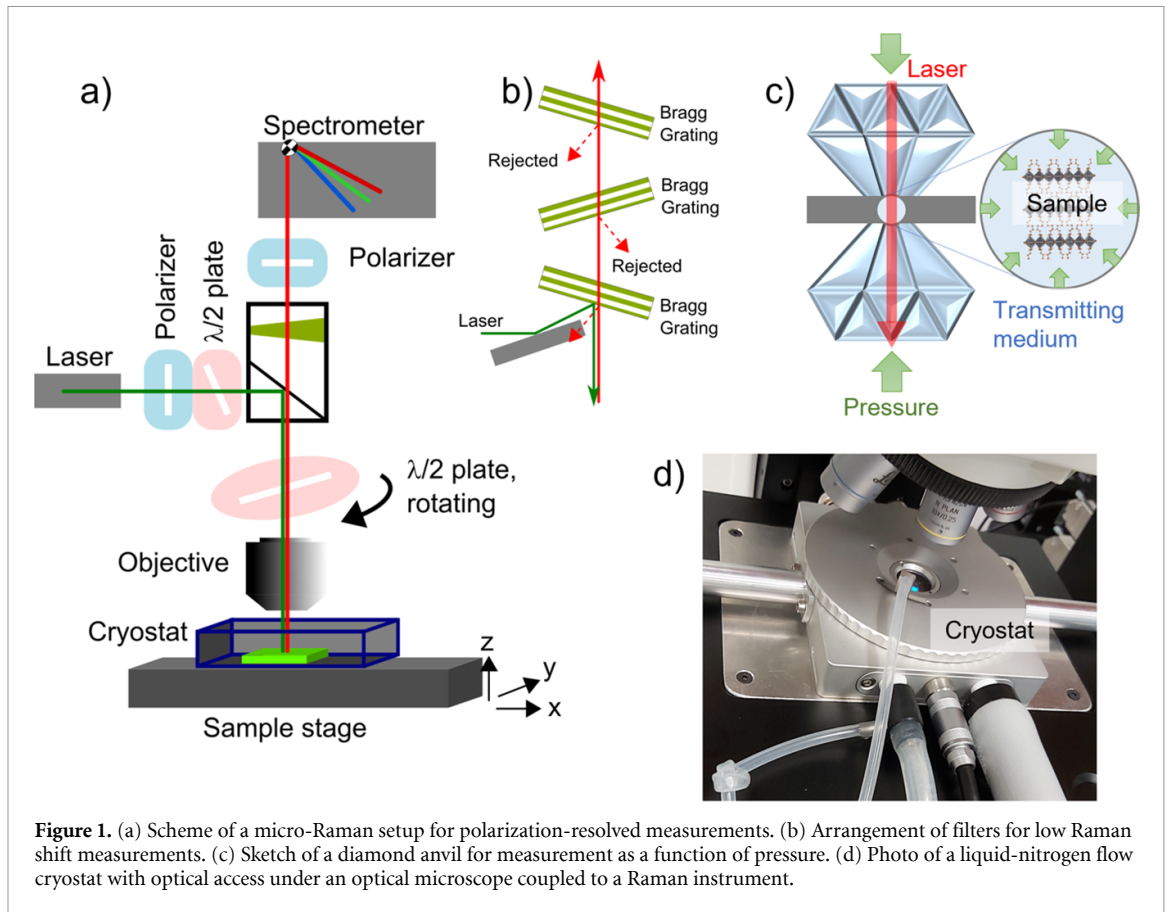


Figure 1. (a) Scheme of a micro-Raman setup for polarization-resolved measurements. (b) Arrangement of filters for low Raman shift measurements. (c) Sketch of a diamond anvil for measurement as a function of pressure. (d) Photo of a liquid-nitrogen flow cryostat with optical access under an optical microscope coupled to a Raman instrument.

crystalline momentum k , energy E (or angular frequency ω) [57, 60, 62]. The modes are classified according to the point group associated to the value of k and each can be assigned an irreducible representation of the point group; for phonons at the zone centre ($k = 0$), the point group coincides with the point group of the crystal class. Since Raman scattering requires conservation of E and k , and the incoming phonons can be approximated as having zero momentum, the phonon modes observed in Raman spectroscopy at the 1st order are those at $k = 0$, and with an energy different from 0. The symmetry of the vibration (its irreducible representation) determines the Raman activity of the mode, and its polarization selection rules, i.e. whether a certain mode has a non-zero intensity in Raman scattering with defined polarization of incident and scattered light. The selection rules are summarized in the ‘Raman tensor’. The intensity of a mode (I) is $I \propto |e_s R e_i|^2$, where e_s , e_i are the polarization vectors of the scattered and incident light, and R is the Raman tensor. The most general Raman tensor, R , has nine components. In case of non-resonant scattering (i.e. excitation far from an absorption peak), the tensor is symmetric. The number of independent components is determined by the irreducible representation associated to the mode; these Raman tensors are tabulated in the literature for each point group [60, 62, 63].

Polarized Raman spectroscopy is thus very effective in the assignment of the symmetry (i.e. irreducible representation) to the mode, provided that the orientation of the crystal is controlled. The information on orientation of the crystal and of the polarization vector are often reported in the Porto notation as $k_i(e_i, e_s)k_s$, where the four symbols indicate the direction and of incident and scattered photons, (k_i and k_s) and their respective polarization direction (e_i and e_s). In this way, the notation $z(yx)y$ indicates a scattering with light incoming from z and observed along y , and with incoming polarization along y , and observed with a polarization along x . The directions xyz usually refer to the crystal axes. For the typical backscattering geometry of figure 1(a), the direction k_s is labelled as \bar{z} indicating $-z$; in this way, a configuration may be $z(yx)\bar{z}$. The selection of orientation is especially easy and powerful in layered materials, whose cleaving occurs in the stacking direction [64–66]. The experimental study of the symmetry requires the rotation of the polarization of the incident and/or the scattered light, and can be obtained in different optical configurations [67], such as rotating the sample, while keeping fixed polarizers, or rotating the excitation polarization. In figure 1(a), a set-up is shown including a rotating half-wave ($\lambda/2$) plate that rotates both incident and scattered light; the incoming polarization can be controlled with another waveplate, while the analyser at the spectrometer is fixed. In these experiments, the intensity of each Raman mode can be measured as a function

Table 1. Summary of Raman spectroscopy studies on 3D HOIPs indicating the compound used, details of the technique and available information about assignment of modes and phase transitions.

Compound ^a	Details of Raman measurement	Available information	References
MAPbI ₃	Room temperature	MA mode assignment, comparison with DFT	Quarti <i>et al</i> [80]
MAPbI ₃ MAPbI _{3-x} Br _x (<i>x</i> = 0–1)	Room temperature Low frequency	Inorganic peaks, effect of composition, comparison with Pb salts	Ledinský <i>et al</i> [48]
MAPbI ₃	Different excitation laser	Deconvolution of modes associated to organic and inorganic part; effect of laser exposure	Pistor <i>et al</i> [50]
MAPbI ₃	Pressure dependent	Phase transition with pressure	Francisco-López <i>et al</i> [81]
MAPbI ₃	Temperature-dependent Polarization	Detailed mode assignment by comparison with DFT	Pérez-Osorio <i>et al</i> [82]
MAPbI ₃	Temperature dependent Polarization angle dependent	Mode assignment from polarization dependence	Sharma <i>et al</i> [83]
MAPbX ₃ (X = I, Br, Cl)	Temperature dependent	Detailed mode assignment and effect of halide, comparison with DFT	Leguy <i>et al</i> [43]
MAPbBr ₃ CsPbBr ₃	Low frequency Temperature dependent	Phase transition	Guo <i>et al</i> [84]
FAPbI ₃ FAPbBr ₃	Low frequency	Detailed mode assignment and effect of composition, comparison with DFT	Ibaceta-Jaña <i>et al</i> [52]
Cs ₂ AgBiBr ₆	Low temperature	Mode assignment	Zelewski <i>et al</i> [85]
Cs ₂ AgBiBr ₆ CsPbBr ₃	Low frequency Temperature dependent Polarization angle dependent	Phase transition and mode symmetry, comparison single and double perovskites	Cohen <i>et al</i> [46]

^a Organic cations notation: MA = methylammonium; FA = formamidinium. Techniques notation: DFT = density functional theory.

of the rotation angle, for configurations where the laser and the analyser polarization are parallel or perpendicular. This configuration is preferred as it does not require moving the sample, thus ensuring that the investigated spot remains the same during the polarization angle-dependent measurement. These methods have provided interesting information on 2D materials, including crystallographic orientation, strain status, and inter- and intra-layer interactions in heterostructures such as Moiré patterns [64, 66].

Raman spectroscopy is also often coupled to microscopes for spatially resolved studies with resolution of hundreds of nanometres. Pressure- and temperature-dependence measurements, which are very relevant in the study of phase transitions as described in section 4, can be measured in systems with optical access, which can be easily integrated in spectroscopy setups. These include diamond anvil cells (DACs) and cryostats (figures 1(c) and (d)). Anvil cells exploit the transparency of diamond to visible light for spectroscopic access, and can apply uniaxial stress as well as isotropic stress with a pressure transmitting medium, such as silicone oil [68, 69] or NaCl [70], and calibrate the pressure using ruby [68, 70]. Cryostats with optical access can be He- or liquid-N₂ cooled allowing to reach temperatures in the range 4–350 K.

In tables 1 and 2, we show a summary of the reported works with 3D and layered HOIPs indicating the technique used and the aim of the study, respectively.

3. Inorganic and organic Raman features

From a qualitative point of view, the vibrational modes in the layered HOIPs can be divided between those related to the organic part and those related to the inorganic part. The organic cation-related vibrations typically occur at higher Raman shift (>300 cm⁻¹), and several modes can be expected. These can then be qualitatively matched to the typical spectra for the molecular species, which can be found in the literature [71]. In this case, well-established spectroscopy practice identifies the modes related to chemical bonds in functional groups according to their Raman shift [71]. For the inorganic case, the modes are found at lower energy, due to the heavier atomic components [62]; typically, these modes can be directly mapped to the 3D counterparts, and their symmetry matches that of the octahedra. This simple classification assumes a

Table 2. Summary of Raman spectroscopy studies on layered HOIP reported indicating the compound used, aim of the work and details of the technique, and available complementary methods.

Compound ^a	Type of perovskite	Target	Details of Raman measurement	Complementary techniques	References
(BA) ₂ PbI ₄ (EDBE) ₂ PbI ₄	Ruddlesden-Popper <i>n</i> = 1	<ul style="list-style-type: none"> • Effect of octahedral distortions in defects and charge relaxation dynamics • Structural differences between the crystals • Formation of colour centres • Access and assign vibrational motions 	Room-temperature	XRD PL Absorbance DFT calculations of density of states	Cortecchia <i>et al</i> [86]
(BA) ₂ PbI ₄ (PEA) ₂ PbI ₄	Ruddlesden-Popper <i>n</i> = 1	<ul style="list-style-type: none"> • Determine organic cations rearrangement and inorganic octahedra distortion/tilting under pressure. 	<ul style="list-style-type: none"> • Non-resonant • temperature-dependent • Low-frequency • Pressure-dependent • Low-frequency modes (0–80 cm⁻¹) 	DFT calculations for Raman spectrum	Dragomir <i>et al</i> [87]
(BA) ₂ PbI ₄	Ruddlesden-Popper <i>n</i> = 1	<ul style="list-style-type: none"> • Molecular level explanation of dual band emission (caused by exciton-phonon coupling) • Determine the responsible vibrations for exciton-phonon coupling • Determine phase transition 	<ul style="list-style-type: none"> • Temperature-dependent 	Pressure-dependent absorbance, steady-state and time-resolved photoluminescence and XRD. Band structure calculations. <ul style="list-style-type: none"> • Temperature-dependent and time-resolved PL • Steady state PL and PLE • FTIR • Time-correlated single-phonon counting (TCSPC) • Absorbance • Temperature-dependent powder XRD 	Yin <i>et al</i> [88]
(BA) ₂ PbI ₄	Ruddlesden-Popper <i>n</i> = 1	<ul style="list-style-type: none"> • Comparison of vibrational symmetries of 2D and 3D crystals in temperature. • Order-disorder phase transition 	<ul style="list-style-type: none"> • Polarization • Low-frequency • Temperature-dependent 	Temperature-dependent XRD DFPT calculations of Raman modes	Moral <i>et al</i> [89]
(BA) ₂ PbI ₄ (PEA) ₂ PbI ₄	Ruddlesden-Popper <i>n</i> = 1	<ul style="list-style-type: none"> • Comparison of vibrational symmetries of 2D and 3D crystals in temperature. • Order-disorder phase transition 	<ul style="list-style-type: none"> • Polarization • Low-frequency • Temperature-dependent 	Temperature-dependent XRD DFPT calculations of Raman modes	Menahem <i>et al</i> [79]

(Continued.)

Table 2. (Continued.)

Compound ^a	Type of perovskite	Target	Details of Raman measurement	Complementary techniques	References
(C _x H _{2x+1} NH ₃) ₂ PbI ₄ (x = 4–9)	Ruddlesden-Popper n = 1	<ul style="list-style-type: none"> Investigate the modular structural tunability by varying the length of the carbon chain (x) of the alkylammonium cation Determine the vibrational modes coupled to the excited-state potential energy surface Exciton-phonon interaction evaluation 	<ul style="list-style-type: none"> Low-frequency Resonant impulsive-stimulated Raman scattering (RISRS) Temperature-dependent 	<ul style="list-style-type: none"> Powder and film XRD Temperature-dependent PL Femtosecond transient absorption DFT for lattice dynamics simulations (frequencies and assignment) 	Mauck et al [78]
(BA) ₂ (MA) _{n-1} Pb _n I _{3n+1} n = 2–4	Ruddlesden-Popper (n = 2–4)	<ul style="list-style-type: none"> Measure and assign low frequency Raman modes 	<ul style="list-style-type: none"> Low frequency Temperature-dependent 	<ul style="list-style-type: none"> DFT calculations of Raman modes 	Dahod et al [90]
(BA) ₂ (FA)Pb ₂ I ₇ (PA) ₂ (MA)Pb ₂ I ₇ (HA) ₂ (MA)Pb ₂ I ₇ (HA) ₂ PbI ₄ (HA) ₂ PbBr ₄ (BA) ₂ PbI ₄ (BzA) ₂ PbI ₄	Ruddlesden-Popper n = 1	<ul style="list-style-type: none"> Characterization of Raman modes and dependence with the metal halide Study the coupling between organic and inorganic layers 	<ul style="list-style-type: none"> Polarization Temperature-dependent 	DFT and DFPT calculations for crystallography and Raman modes Powder XRD	Lavan et al [91]
(PEA) ₂ PbI ₄	Ruddlesden-Popper n = 1	Determine molecular interlayer interactions and orientation of the PEA cations under pressure.	<ul style="list-style-type: none"> Pressure-dependent Low-frequency modes (0–80 cm⁻¹) 	Pressure-dependent photoluminescence and XRD. Band structure calculations. Pressure-dependent PL. DFT Raman modes calculations.	Liu et al [69]
(BA) ₂ MAPb ₂ I ₇	Ruddlesden-Popper n = 2	Determine organic cations rearrangement under pressure.	<ul style="list-style-type: none"> Pressure-dependent 	Pressure-dependent PL.	Yin et al [92]
(NA) ₂ PbI ₂ Br ₂	Ruddlesden-Popper n = 1	<ul style="list-style-type: none"> Determine phase transition Conformation of alkyl chain Gain information on the crystal dynamics Degree of disorder Mechanisms involved in the transition 	<ul style="list-style-type: none"> Temperature-dependent 	<ul style="list-style-type: none"> DSC Temperature-dependent powder XRD FTIR spectroscopy 	Abid et al [93]

(Continued.)

Table 2. (Continued.)

Compound ^a	Type of perovskite	Target	Details of Raman measurement	Complementary techniques	References
(BA) ₂ PbBr ₄ (PEA) ₂ PbBr ₄	Ruddlesden-Popper <i>n</i> = 1	<ul style="list-style-type: none"> Study of the directionality of the fundamental phonon modes depending on the organic part, temperature and polarization. Control of vibrational modes coupling using polarization 	<ul style="list-style-type: none"> Low frequency Polarization Temperature-dependent 	AFM XRD Absorbance DFT calculations of Raman modes PL	Dhanabalan et al [94]
(BA) ₂ PbBr ₄ (BA) ₂ MAPb ₂ Br ₇	Ruddlesden-Popper <i>n</i> = 1 and 2	Determine inorganic octahedra distortion/tilting under pressure.	<ul style="list-style-type: none"> Pressure-dependent Low-frequency modes (0–80 cm⁻¹) 	Pressure-dependent photoluminescence. Band structure and bandgap calculations.	Li et al [70]
(HA) ₂ GAPb ₂ Br ₇	Ruddlesden-Popper <i>n</i> = 2	Determine inorganic octahedra distortion/tilting under pressure.	<ul style="list-style-type: none"> Pressure-dependent Low-frequency modes (0–120 cm⁻¹) 	Pressure-dependent UV–Vis absorption and PL spectroscopy. High-pressure synchrotron XRD measurements.	Guo et al [95]
(BA) ₂ PbBr ₄ (UDA) ₂ PbBr ₄ (MDA) ₂ PbBr ₄ (MDDA) ₂ PbBr ₄	Ruddlesden-Popper <i>n</i> = 1	<ul style="list-style-type: none"> Investigation with different organic moieties towards white light emission Resolving uniaxial and biaxial symmetries of the in-plane components Insight into the dynamics of the white emission of these materials 	<ul style="list-style-type: none"> Polarized angle-resolved Temperature-dependent Low-frequency 	Band structure DFT calculations. Temperature-dependent PL DFT calculations of Raman modes	Lin et al [76]
(PA) ₄ AgBiBr ₈ (BA) ₄ AgBiBr ₈ (PEA) ₄ AgBiBr ₈ (PA) ₂ CsAgBiBr ₇ (BA) ₂ CsAgBiBr ₇ (PEA) ₂ CsAgBiBr ₇ (3cp)PbBr ₃	Ruddlesden-Popper <i>n</i> = 1 <i>n</i> = 2 double perovskites Post-perovskite, <i>n</i> = 1	<ul style="list-style-type: none"> Determine phase transition varying the organic cation Investigation of asymmetry Determine phase transition 	<ul style="list-style-type: none"> Temperature-dependent Polarization Temperature dependent 	Temperature-dependent absorbance and PL Band structure DFT calculations XRD Temperature-dependent PL and PLE Band structure DFT calculations XRD	Martín-García et al [77] Selivanov et al [96]

^a Organic cations notation: MA = methylammonium; FA = formamidinium; GA = guanidinium; PA = propylammonium; BA = butylammonium; NA = nonylammonium; UDA = undecylammonium; MDA = methyldecylammonium; MDDA = methyldecylammonium; PEA = phenethylammonium; BzA = benzylammonium; EDDBE = 2,2-(ethylenedioxy)-bis(ethylammonium); 3cp = 3-cyanopyridinium. Experimental techniques notation: DSC = differential scanning calorimetry; PL = photoluminescence; PLE = photoluminescence excitation; FTIR = Fourier-transform infrared; XRD = x-ray diffraction; DFT = density functional theory; DFPT = density-functional perturbation theory.

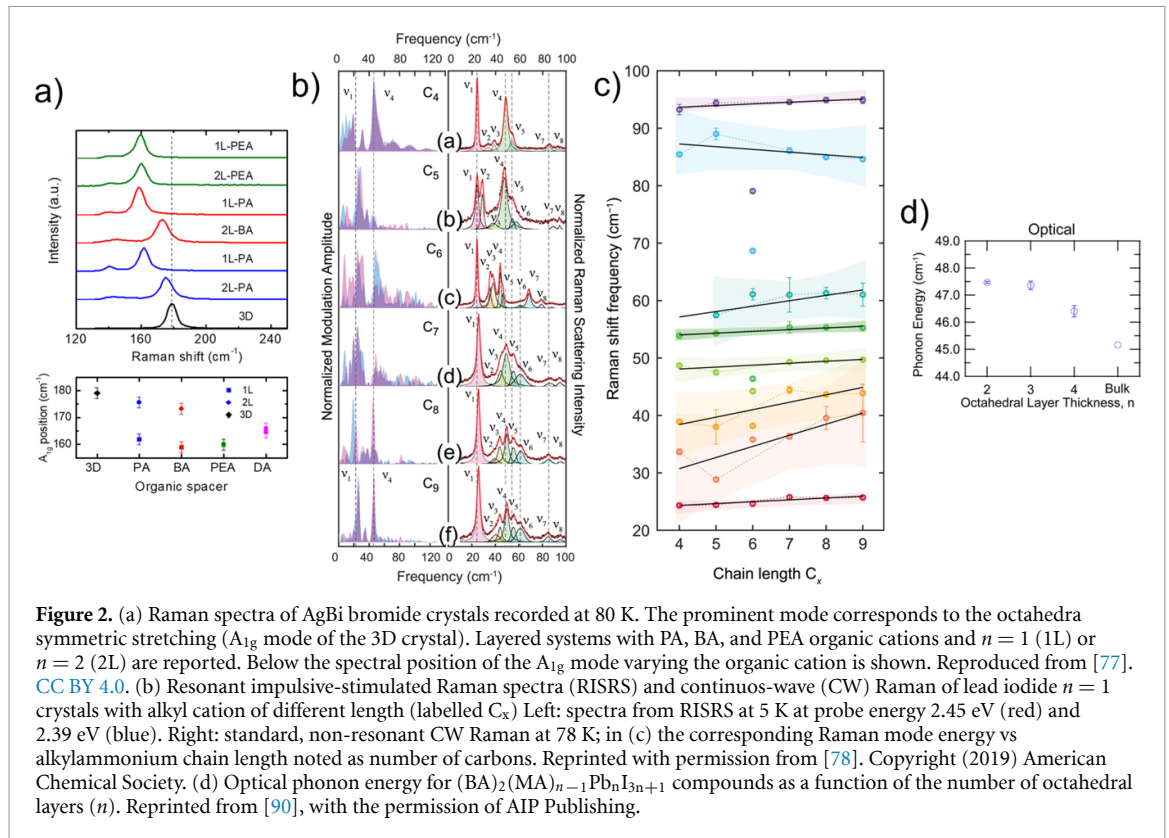


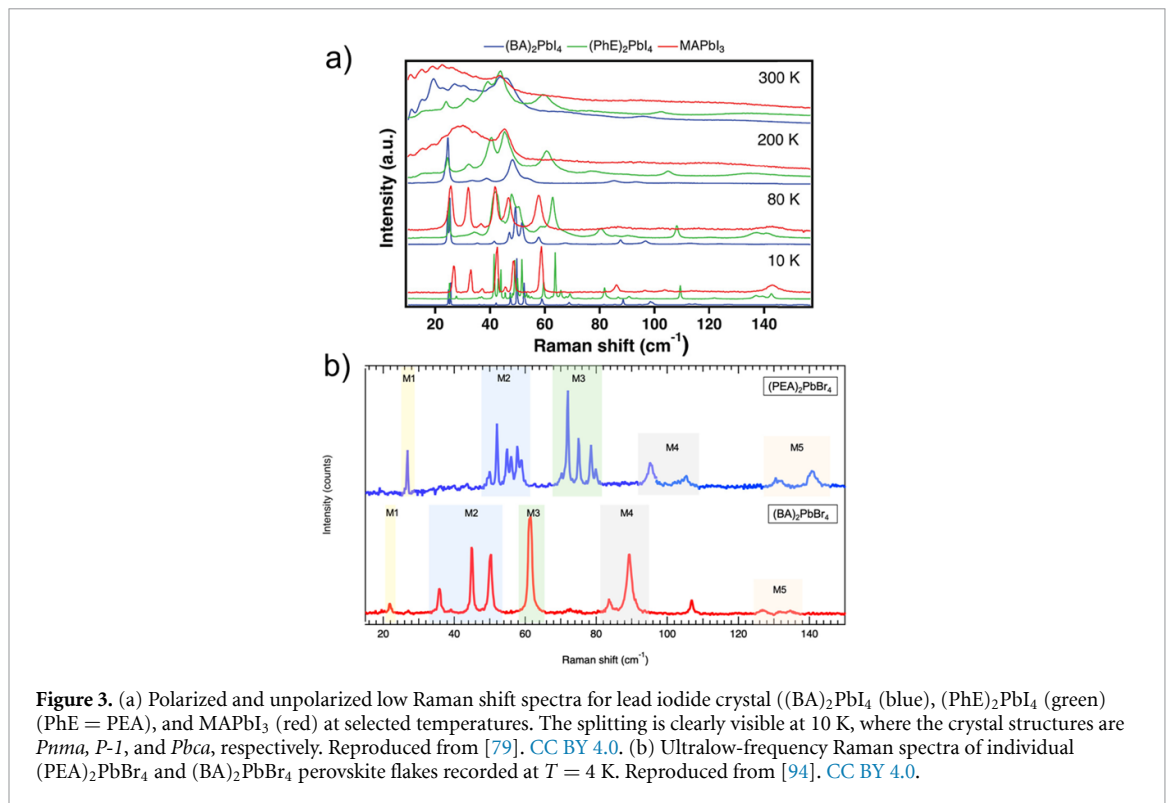
Figure 2. (a) Raman spectra of AgBi bromide crystals recorded at 80 K. The prominent mode corresponds to the octahedra symmetric stretching (A_{1g} mode of the 3D crystal). Layered systems with PA, BA, and PEA organic cations and $n = 1$ (1L) or $n = 2$ (2L) are reported. Below the spectral position of the A_{1g} mode varying the organic cation is shown. Reproduced from [77]. CC BY 4.0. (b) Resonant impulsive-stimulated Raman spectra (RISRS) and continuous-wave (CW) Raman of lead iodide $n = 1$ crystals with alkyl cation of different length (labelled C_x) Left: spectra from RISRS at 5 K at probe energy 2.45 eV (red) and 2.39 eV (blue). Right: standard, non-resonant CW Raman at 78 K; in (c) the corresponding Raman mode energy vs alkylammonium chain length noted as number of carbons. Reprinted with permission from [78]. Copyright (2019) American Chemical Society. (d) Optical phonon energy for $(BA)_2(MA)_{n-1}Pb_nI_{3n+1}$ compounds as a function of the number of octahedral layers (n). Reprinted from [90], with the permission of AIP Publishing.

negligible interaction between the molecular cations and the inorganic octahedra, which can be justified taking into account the localized nature of the vibration of heavy atoms [72, 73], but it does not describe the real scenario, which is more complex.

Typically, HOIP lattices are much softer than other inorganic semiconductors, i.e. the displacement of the ions from their equilibrium positions requires little energy. As a result, the lattice dynamics occurs with large ion displacement, which results in highly anharmonic vibrations, especially at room temperature [73]; for this reason, the phonon propagation is short, and the vibrations occur as localized modes. The localized nature of the modes almost decouples the motion of the different parts in the complex unit cell, such as the inorganic cage and the organic moieties. This has been observed in lead-based [74, 75] and in lead-free compounds [73]. In this sense, the study of Raman spectroscopy provides further insight into the nature of the modes, especially by identifying their symmetry with polarization selection rules and by analysing temperature (and pressure) dependence. The effect of localized modes is particularly striking in the 2D HOIPs, where the vibrations of the inorganic part retain their feature, e.g. in terms of symmetry and Raman selection rules, even in lower symmetry environment [76]. Additionally, the long organic molecules in the 2D HOIPs ‘enhance’ the relevance of anharmonic effects, as the inorganic layers are more decoupled by each other. This is relevant in phase transitions and in the study of electron-phonon coupling, as discussed in sections 4 and 5.

As an example of the interplay between the organic cations and the inorganic lattice, we consider the double perovskites (figure 2(a)) of the AgBi bromide HOIP family [77], which can be synthesized with $n = 1$ and 2, being the 3D counterpart $Cs_2AgBiBr_6$. While the organic moieties give rise to a variety of peaks, the stronger feature in the range of inorganic vibration corresponds to the A_{1g} mode of the 3D case, ascribed to a symmetric stretching of the octahedra in the lattice. In the layered crystals with $n = 1$, this Raman band is found to have similar value across samples with different organic cations, comprising the alkylammonium cations propyl- (PA), butyl- (BA) and decyl-ammonium, as well as the aromatic phenylethylammonium (PEA). Instead, in the $n = 2$ structures, the mode’s frequency decreases with increasing alkyl chain length, while for PEA a value comparable with $n = 1$ case is found. A comparison with the same symmetric stretching mode of the 3D $Cs_2AgBiBr_6$ indicates that in layered structures the phonon frequency (energy) is reduced, and that in the $n = 1$ materials the frequency (energy) is lower than in $n = 2$. This can be attributed to the higher stiffness of materials with a larger number of layers.

Systematic studies have explored the effect of the organic cation’s nature and volume on the vibrational modes of the inorganic layers, in terms of Raman shift and linewidth. For instance, Mauck *et al* [78] have studied lead iodide with alkylammonium cations with carbon chains of different lengths, x , (x from 4 to 9),

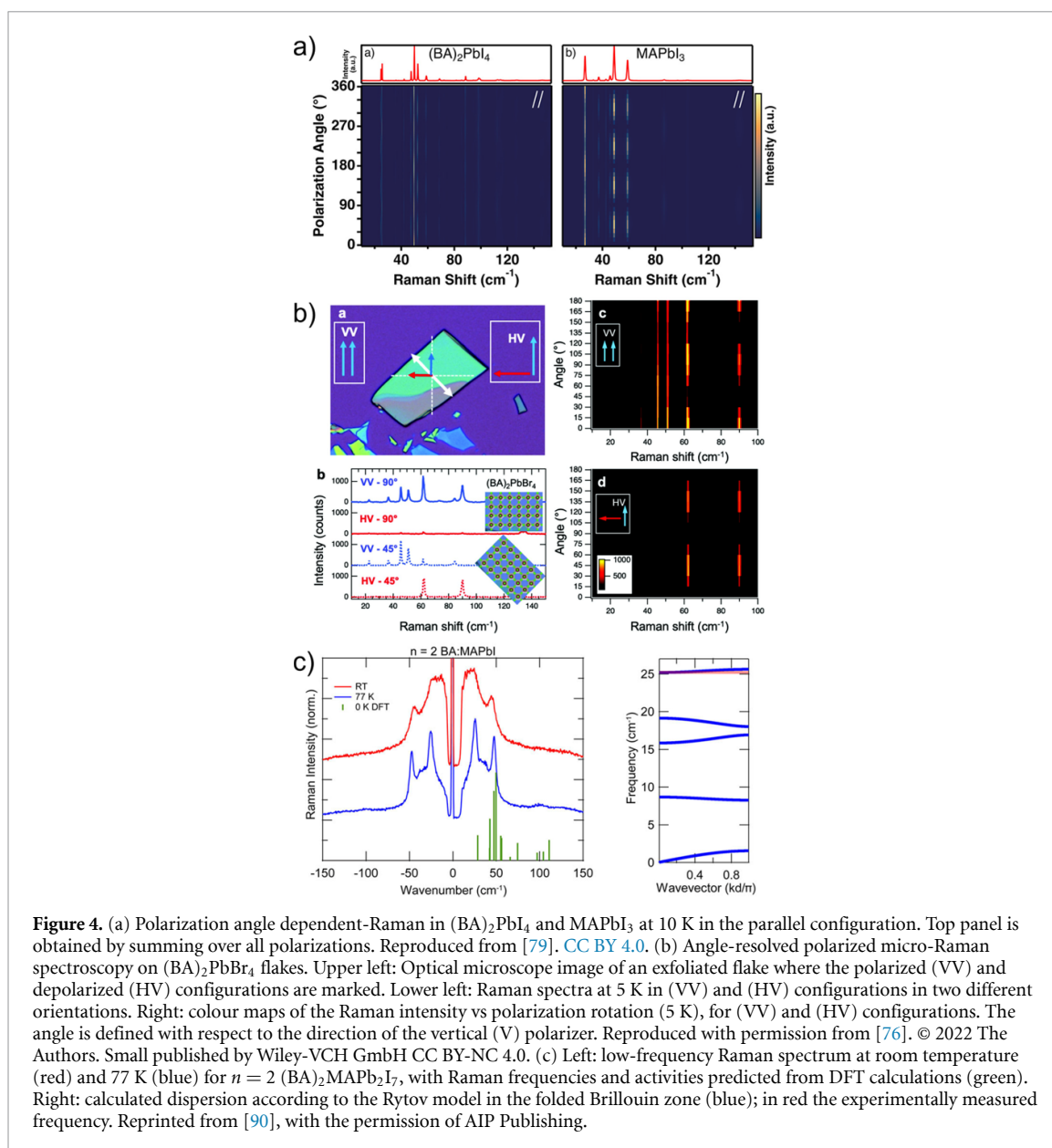


focusing on the monolayer ($n = 1$) case (figures 2(b) and (c)). These compounds crystallize in the same monoclinic $P2_1/c$ space group, except $x = 6$, which belongs to the orthorhombic *Pbca*. It is important to note that the crystal structure may be strongly affected by the organic cation, as seen in figure 3(a), which compares the 3D lead iodide with methylammonium (MA) to its layered counterparts using BA and PEA as organic cations [79]. In [78], the Raman modes associated with octahedral vibrations are found to have a small blue or redshift for increasing chain length, with an approximately linear relation (with deviation for $x = 6$). However, the dependence is not the same for all modes, as some of them increase their energy for longer chains and others decrease it, highlighting that it is not a straightforward relationship, as well as the sensitivity of Raman spectroscopy to detect these changes.

On the other hand, in the case of an optical mode associated with a twisting of the octahedra in (BA)₂MAPbI₄ (figure 2(d)), an increase in the number of octahedra in the lattice reduces the frequency (energy), with the bulk having the minimum value [90]. Here, this effect is rationalized as the interaction between octahedra directly bonded to the organic cations, and those that have only inorganic moieties around them, the latter being associated to lower energy as in the bulk.

Additionally, it is worth noting that the inorganic cage can leave enough space to allow the movement of the organic A-cation, especially at room temperature, which results in polar fluctuation and, in the spectra, in a broad zero-energy peak, which is observed in 3D and 2D cases [90, 97]. In some cases, at low temperature the modes related to the motion of the whole organic cation (translation/libration, spinning) can be observed at low energy [82]. An effective way to evaluate the effect of the organic cation's nature and volume on the vibration modes of the inorganic layers for a specific lattice is to quantify the octahedral distortion in the crystal structure in terms of the $M \cdots X$ bond length and angle compared to the ideal octahedron, since both parts are assembled by hydrogen bonding. This can be done using the mean octahedral quadratic elongation (λ_{oct}) and the octahedral angle variance (σ_{oct}^2) [77, 86, 98], following the equations: $\lambda_{oct} = \frac{1}{6} \sum_{i=1}^6 \frac{\ell_i}{\ell_0}$ and $\sigma_{oct}^2 = \frac{1}{11} \sum_{i=1}^{12} (\alpha_i - 90^\circ)^2$, where ℓ_0 and ℓ_i are the $M \cdots X$ bond lengths in a regular octahedron and the studied octahedron, respectively, and α_i the $X \cdots M \cdots X$ angles. In this way, a shift towards lower frequency (energy) values for the octahedra-related modes is generally observed when increasing the octahedral distortion [77, 86].

As discussed in the previous section, the crystal symmetry of 2D HOIP is typically tetragonal, orthorhombic, triclinic, or monoclinic. When the lattice symmetry is reduced from cubic or tetragonal in the 3D cases, to orthorhombic or triclinic or monoclinic, a splitting can be expected for each degenerate mode. Indeed, the appearance of new modes at low energy in layered HOIP can be directly described in these terms. The splitting is related to the coupling with the molecular cations and can be related to a difference in the



stiffness of the organic part. When the cations interact strongly, as in the case of aromatic cations, the stiffer organics will lead to a less symmetric structure, with the appearance of several Raman active modes. This was shown by Menahem *et al* [79], who compared BA, MA and PEA lead iodide with $n = 1$ (figure 3(a)), and Dhanabalan *et al* [94] have shown how PEA and BA have different effects on the spectrum of lead bromide $n = 1$ 2D HOIP (figure 3(b)). As PEA is stiffer, more modes are observed at low energy with respect to the softer BA. This was ascribed to a stronger coupling between octahedra due to the rigid PEA.

The symmetry assignment of the Raman modes is based on two complementary methods. The use of numerical methods such as density functional theory (DFT) allow finding the normal vibrational modes, including their expected range of frequency (energy), and intensity. Finally, the symmetry of the mode can be assessed by direct calculation of the Raman tensor as the derivative of the polarizability with respect to the normal mode [76, 78, 79, 93, 94]. DFT methods predict a large number of vibrational modes in HOIPs, as expected due to the large number of atoms in the unit cell. In these simulations, the effect of the low symmetry of the crystal is clearly visible together with the effect of the interaction between the organic and inorganic parts.

From the experimental side, polarization-resolved Raman spectroscopy measurements allow to identify the symmetry of each mode, which can be matched with an analysis of the symmetry of the crystal. An example of the experimental polarization-dependent results is shown in figure 4(a), for BA_2PbI_4 (layered HOIP with $n = 1$) and MAPbI_3 (3D). The colour maps highlight the 4-fold symmetry for the vibrational modes of the inorganic cage, associated with the symmetry of orthorhombic lattices. Interestingly, similar

symmetry is found in crystals without 4-fold axes, such as the monoclinic $(\text{UDA})_2\text{PbBr}_4$ [76]. There, the pattern results from the symmetry of the octahedra, due to the localized nature of the modes. Additionally, the organic cation can affect the polarization dependence. In [94], a band assigned to Pb–Br scissoring has a distinct anisotropy with PEA but not with BA, suggesting an effect of the relative orientation of the phenyl ring and the inorganic octahedral lattice. This anisotropy appears as a band found in depolarized spectrum of PEA crystal, but not in the corresponding polarized spectrum.

The anisotropic response is even more striking in cases where the plane of inorganic octahedra is very relevant. This occurs in materials that present the so-called ‘post-perovskite’ structure, which is strikingly different from Ruddlesden-Popper (RP) and Dion-Jacobson (DJ). Here, the octahedra share a corner in one direction (y) and share an edge in the orthogonal direction (x). As shown in Selivanov *et al* [96], Raman spectra with parallel polarization xx and yy will be different, being stronger in the direction of the corner sharing octahedra since the vibration amplitude is larger.

The low energy range is particularly interesting as it can host modes associated to a variety of phenomena, as has been demonstrated for other materials [99]. Global vibrations of nanoparticles, such as breathing of carbon nanotubes [62] or breathing of 2D CdSe nanomaterials [100–103], can be found here. In the case of layered structures, such as semiconductor superlattices [104] and 2D HOIPs, vibrations with long wavelength can be associated to the periodicity of the stack of the layers, in analogy with multi quantum wells [90]. They arise from the longitudinal acoustic waves of the individual layers, which are folded in the ‘mini Brillouin zone’ of the superlattice, yielding ‘phononic minibranches’. In 2D HOIPs, different elastic properties of the inorganic and organic parts would give rise to well-separated minibranches. Dahod *et al* [90] have analysed the low energy spectrum of $(\text{BA})_2\text{MAPb}_2\text{I}_7$ with $n = 2$ following this model, as shown in figure 4(c). In particular, they assumed that the velocity of sound in the organic and inorganic parts is the same as in the bulk and used a continuum approximated model (the Rytov model [104]) to calculate the zone-folded longitudinal acoustic modes (zf-LA) expected in a superlattice. This result is used to explain the appearance of a peak at $\sim 25 \text{ cm}^{-1}$, whose experimental high intensity was not predictable by DFT. This assignment, although not conclusive, is supported by the dependence of this mode on the choice of the organic moieties and of the number of octahedral layers (n) of the inorganic lattice. Nonetheless, it is interesting to note that this interpretation of the low-frequency mode is in stark contrast to a motion of the heavy ion, the latter being typically local, while the former is long-ranged by definition. The difference can be quite important in the interaction with electrons, as discussed in section 5, because of the relevance of the lattice distortion generated in the two cases, that can lead to different optical properties. This further highlights the need for a proper identification of vibrational modes in these materials. Table 3 contains a summary of the vibrational modes described in the literature for layered HOIPs.

Another important case of modes at low energy is related to soft modes in phase transitions, discussed in the following section.

4. Phase transitions

The hybrid nature of these materials plays a key role in the phase transition, which results from the coupling between the structural modulation of the inorganic octahedra layer and the conformational flexibility of the organic cations, both connected by hydrogen-bonding interactions at the R-NH_3^+ moiety. The phase transitions can occur as related to the order state of the organic moieties [77]; in this case, the discontinuous nature is clearly evident in the Raman spectrum of the inorganic part as a ‘jump’ in peak position and linewidth, while in the organic part a transition from ‘solid-like’ (narrow peaks) to ‘liquid-like’ (broad peaks) is observed. This leads to strong distortion (tilting) of the inorganic octahedra [77, 79], affecting the optoelectronic properties. This mechanism is slightly different from the case of 3D HOIPs; in that case, it has been pointed out that octahedral tilting is responsible for the phase transition as well as for the strong anharmonicity [105]. In this way, the inorganic composition (metal and halide) and the organic cation nature ($\text{R} =$ alkyl chains, aromatic, or more complex molecules) determine the phase transition temperature of the resulting compound. Therefore, it is possible to establish some general rules. Fixing the metal halide (e.g. PbI_4^- , AgBiBr_8^{4-}) and varying the organic spacer, it has been observed that the phase transition temperature progressively increases with the number of carbon atoms, x , in alkyl ammonium cations, $\text{C}_x\text{H}_{2x+1}\text{NH}_3^+$, and when using aromatic molecules such as PEA. To cite some examples, in the case of the most studied lead halide HOIPs, different reports have shown this trend in the transition temperature: $(\text{PA})_2\text{PbI}_4 \sim 200\text{--}250 \text{ K}$ [106] $<$ $(\text{BA})_2\text{PbI}_4 \sim 250\text{--}270 \text{ K}$ [107, 108]; for $x > 4$ there is more than one phase transition [78, 108], whereas $(\text{PEA})_2\text{PbI}_4$ [87] shows none. Another example is the AgBiBr_8^{4-} double HOIP: $(\text{PA})_4\text{AgBiBr}_8 \sim 172 \text{ K}$ $<$ $(\text{BA})_4\text{AgBiBr}_8 \sim 282 \text{ K}$ and $(\text{PEA})_4\text{AgBiBr}_8$ does not present phase transition at least up to 330 K [77] (figure 5(a)). Both examples highlight the relevance of the nature of the organic cation. While the alkylammonium chains show a higher conformational and motional freedom, the arrangement of

Table 3. Raman modes assignment to the corresponding inorganic lattice and organic cations in layered HOPs determined combining experiments and theoretical calculations.

Compound ^a	Type of perovskite	Inorganic modes	Organic modes	Reference
(BA) ₂ PbI ₄ (EDBE) ₂ PbI ₄	Ruddlesden-Popper <i>n</i> = 1	99 cm ⁻¹ Pb-I stretching Ammonium moieties coupled with the inorganic part; (BA) ₂ PbI ₄ -116 cm ⁻¹ libration mode; 183 cm ⁻¹ torsional mode // (EDBE) ₂ PbI ₄ -136 cm ⁻¹ libration mode	Range 300–1500 cm ⁻¹ (BA) ₂ PbI ₄ presents the usual modes. In contrast, (EDBE) ₂ PbI ₄ shows additional modes due to the greater interaction with the inorganic cage.	Cortecchia <i>et al</i> [86]
(BA) ₂ PbI ₄ (PEA) ₂ PbI ₄	Ruddlesden-Popper <i>n</i> = 1	(BA) ₂ PbI ₄ 72.32 cm ⁻¹ (A _g) in-phase Pb-I (apical) stretching + octahedral rotation 88.9 cm ⁻¹ (A _g) in-phase Pb-I (apical) stretching + octahedral rotation 99.63 cm ⁻¹ (A _g) out of phase Pb-I (equatorial) stretching 114 cm ⁻¹ (B _{1g}) in-phase Pb-I (equatorial) stretching + PbI ₄ breathing (PEA) ₂ PbI ₄ 78.3 cm ⁻¹ (A _g) in-phase Pb-I stretching + octahedral rotation	(BA) ₂ PbI ₄ 127.5 cm ⁻¹ (B _{3g}) organic torsional 146.5 cm ⁻¹ , 154 cm ⁻¹ (A _g)/(B _{1g}) organic torsional 169 cm ⁻¹ , 178.2 cm ⁻¹ (B _{3g})/(A _g) organic torsional 239.1 cm ⁻¹ , 243 cm ⁻¹ (A _g) torsional of H-N-C-C angle: involved H-bonding (PEA) ₂ PbI ₄ 106.2 cm ⁻¹ (A _g) π-π vibration of PEA 134.6 cm ⁻¹ (A _g) π-π vibration of PEA 139.3 cm ⁻¹ (A _g) π-π vibration of PEA Raman modes related to BA cation: 250–370 cm ⁻¹ CCN twisting/NH ₃ ⁺ deformation 341 and 400 cm ⁻¹ CCN wagging 419 cm ⁻¹ C-N deformation 476 cm ⁻¹ NH ₃ ⁺ twisting/CCN deformation	Dragomir <i>et al</i> [87]
(BA) ₂ PbI ₄	Ruddlesden-Popper <i>n</i> = 1	—	—	Moral <i>et al</i> [89]

(Continued.)

Table 3. (Continued.)

Compound ^a	Type of perovskite	Inorganic modes	Organic modes	Reference
(BA) ₂ PbI ₄ (PEA) ₂ PbI ₄	Ruddlesden-Popper <i>n</i> = 1	(BA) ₂ PbI ₄ — <i>T</i> = 10 K 24.8 cm ⁻¹ (B _{1g}) octahedra tilting in-plane 25.6 cm ⁻¹ (A _g) octahedra tilting in-plane 36.0 cm ⁻¹ (A _g) octahedra tilting in-plane + twisting out-of-plane 42.2 cm ⁻¹ (A _g) octahedra tilting in-plane 47.4 cm ⁻¹ (B _{1g}) octahedra tilting & Pb-I wagging in-plane 49.9 cm ⁻¹ (A _g) octahedra tilting in-plane 52.5 cm ⁻¹ (B _{1g}) octahedra tilting & Pb-I scissoring in-plane 58.9 cm ⁻¹ (B _{1g}) octahedra & Pb-I tilting in-plane + Pb-I scissoring in-plane 68.8 cm ⁻¹ (B _{1g}) Pb-I symmetric stretch scissoring in-plane 72.3 cm ⁻¹ (A _g) Pb-I symmetric stretching 81.5 cm ⁻¹ , 85.4 cm ⁻¹ (B _{1g}) Pb-I symmetric stretching 88.5 cm ⁻¹ (A _g) Pb-I symmetric stretching + antisymmetric stretching in-plane 94.4 cm ⁻¹ (B _{1g}) Pb-I contraction 98.4 cm ⁻¹ (A _g) octahedra tilting + Pb-I antisymmetric stretching in-plane 99.3 cm ⁻¹ (B _{1g}) Pb-I contraction + Pb-I symmetric stretching 112.6 cm ⁻¹ (A _g) octahedra tilting in-plane 114.8 cm ⁻¹ (B _{1g}) octahedra tilting in-plane 116.4 cm ⁻¹ (A _g) octahedra tilting in-plane & out-of-plane 127.0 cm ⁻¹ (B _{1g}) octahedra tilting + scissoring in-plane 146.3 cm ⁻¹ (B _{1g}) octahedra tilting + Pb-I scissoring in-plane 153.5 cm ⁻¹ (A _g) octahedra tilting in-plane + twisting out-of-plane	—	Menahem et al [79]

(Continued.)

Table 3. (Continued.)

Compound ^a	Type of perovskite	Inorganic modes	Organic modes	Reference
(C _x H _{2x+1} NH ₃) ₂ PbI ₄ (x = 4–9)	Ruddlesden-Popper n = 1	Observed modes: x = 4–24.3 (B _{3g}), 33.7, 38.9 (B _{3g}), 48.7 (A _g), 53.9 (B _{3g}), 85.4 & 93.2 (B _{3g}) cm ⁻¹ x = 5–24.4, 28.8, 38, 47.5, 54.3, 57, 89 & 94.4 cm ⁻¹ x = 6–24.6, 35.8, 38.2, 44.2, 46.4, 61, 68.6 & 79.1 cm ⁻¹ x = 7–25.8, 36.4, 44.4, 49.3, 55, 61, 86.1 & 94.5 cm ⁻¹ x = 8–25.6 (B _g), 40, 43.7 (B _g), 49.5 (A _g), 55.3 (A _g), 61 (B _g), 85 & 94.9 (B _g) cm ⁻¹ x = 9–25.7, 40, 43.9, 49.7, 55.2, 61, 84.6 & 94.9 cm ⁻¹ Raman modes < 40 cm ⁻¹ octahedra twisting with motion of the apical I ⁻ Raman modes 40–60 cm ⁻¹ equatorial I ⁻ moving perpendicular to the stacking axis within the inorganic plane Raman modes < 30 cm ⁻¹ no calculated DFT modes to relate (Rytov model applies) Raman modes 30–60 cm ⁻¹ distortions of the inorganic cage Raman modes > 60 cm ⁻¹ TO modes in which the organic and inorganic sublattices exhibit in-plane shearing Raman modes < 500 cm ⁻¹ translations/vibrations of the lead-halogen framework	—	Mauck et al [78]
(BA) ₂ (MA) _{n-1} Pb _n I _{3n+1} n = 2–4 (BA) ₂ (FA)Pb ₂ I ₇ (PA) ₂ (MA)Pb ₂ I ₇ (HA) ₂ (MA)Pb ₂ I ₇	Ruddlesden-Popper n = 2–4			Dahod et al [90]
(HA) ₂ PbI ₄ (HA) ₂ PbBr ₄ (BA) ₂ PbI ₄ (BzA) ₂ PbI ₄	Ruddlesden-Popper n = 1		Raman modes > 500 cm ⁻¹ vibrations/hindered rotations of organic molecules 800–1000 cm ⁻¹ = C–C bending 1400–1600 cm ⁻¹ NH ₃ ⁺ bending, concretely: (HA) ₂ PbI ₄ –1484.7 cm ⁻¹ (B _g); 1553.5 cm ⁻¹ (A _g); 1562.9 cm ⁻¹ (B _g) // (HA) ₂ PbBr ₄ –1496.3 cm ⁻¹ (B _g); 1572.6 cm ⁻¹ (B _g) // (BA) ₂ PbI ₄ –1479.0 cm ⁻¹ (B _{1g}); 1579.2 cm ⁻¹ (B _{1g}) // (BzA) ₂ PbI ₄ –1474.8 cm ⁻¹ (B _{1g}); 1552.7 cm ⁻¹ (B _{1g}) Raman modes > 2850 cm ⁻¹ are H–X (X=C, N) bond stretching	Lavan et al [91]

(Continued.)

Table 3. (Continued.)

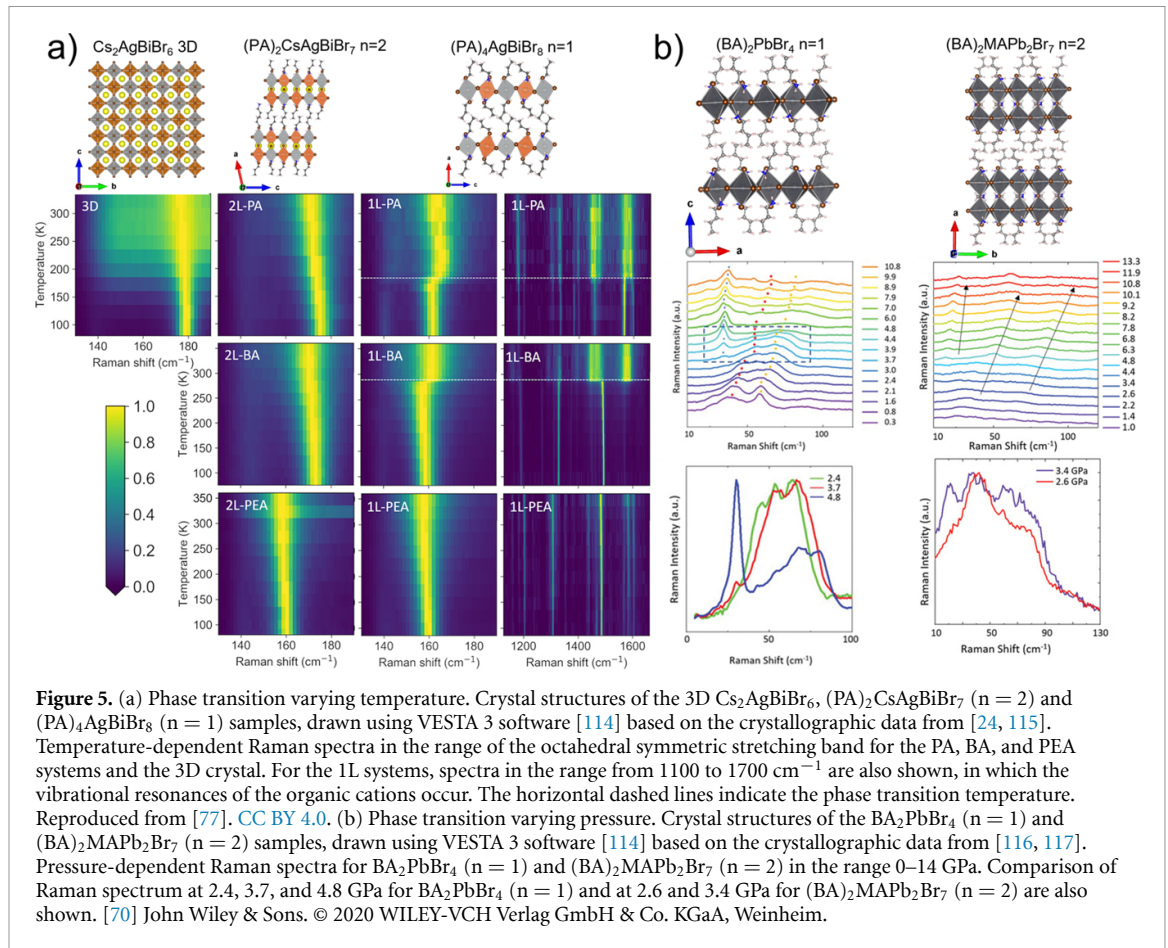
Compound ^a	Type of perovskite	Inorganic modes	Organic modes	Reference
(NA) ₂ PbI ₂ Br ₂	Ruddlesden-Popper <i>n</i> = 1	109 cm ⁻¹ Pb-I Stretching 143 cm ⁻¹ Pb-Br Stretching	401 cm ⁻¹ C-C-N Bending 815 cm ⁻¹ C-C Stretching 883 cm ⁻¹ NH ₃ rocking 1010 cm ⁻¹ CH ₂ Rocking 1075 cm ⁻¹ CH ₃ Rocking 1230 cm ⁻¹ CH ₂ Twisting 1355 cm ⁻¹ CH ₂ Wagging 1458 cm ⁻¹ CH ₂ Scissoring 1565 cm ⁻¹ NH ₃ Deformation 2809 cm ⁻¹ CH ₂ symmetric stretching 2858 cm ⁻¹ CH ₂ Antisymmetric stretching 2960 cm ⁻¹ CH ₃ Symmetric stretching 3024 cm ⁻¹ CH ₃ Antisymmetric stretching 0 GPa - ~475.3 and 484.7 cm ⁻¹ (CCC) & (CCN) bending; ~864.7 cm ⁻¹ BA rocking; ~837.2 cm ⁻¹ CH ₂ rocking —	Abid <i>et al</i> [93]
(BA) ₂ MAIPb ₂ I ₇	Ruddlesden-Popper <i>n</i> = 2	—		Yin <i>et al</i> [92]
(BA) ₂ PbBr ₄ (PEA) ₂ PbBr ₄	Ruddlesden-Popper <i>n</i> = 1	(BA) ₂ PbBr ₄ <i>T</i> = 4 K 21.8 cm ⁻¹ octahedra rocking/twisting (B _{1g} , B _{3g}) 35.7, 44.9, 50.3 cm ⁻¹ Pb-Br bond bending (A _g) 61.5 cm ⁻¹ Pb-Br bond bending and twisting; Br-Pb-Br scissoring in the octahedral plane (B _{2g}) 83.6, 89.1 cm ⁻¹ out-of-plane Pb-Br bond stretching (A _g) 106.8, 132 cm ⁻¹ in/out-of-plane Pb-Br bond stretching (A _g) (PEA) ₂ PbBr ₄ <i>T</i> = 4 K 26.8 cm ⁻¹ octahedra rocking/twisting (B _{1g} , B _{3g}) 52.4, 54.9, 56.0, 57.7, 58.8 cm ⁻¹ Pb-Br bond bending (A _g) 70.3, 72.0, 75.0, 78.5, 80 cm ⁻¹ Pb-Br bond bending and twistings; Br-Pb-Br scissoring in the octahedral plane (B _{2g}) 95.1, 105.3 cm ⁻¹ out-of-plane Pb-Br bond stretching (A _g) 131.6, 140.7 cm ⁻¹ in/out-of-plane Pb-Br bond stretching (A _g)		Dhanabalan <i>et al</i> [94]

(Continued.)

Table 3. (Continued.)

Compound ^a	Type of perovskite	Inorganic modes	Organic modes	Reference
(BA) ₂ PbBr ₄	Ruddlesden-Popper <i>n</i> = 1	25–35 cm ⁻¹ (Rytov model)	—	Lin et al [76]
(UDA) ₂ PbBr ₄		40–50 cm ⁻¹ Pb–Br bond bending and scissoring		
(MDA) ₂ PbBr ₄		50–60 cm ⁻¹ Pb–Br stretching		
(MDDA) ₂ PbBr ₄		80–120 cm ⁻¹ out-of-plane vibrations (e.g. Pb–Br stretching in the cross plane)		
(PA) ₄ AgBiBr ₈	Double perovskites Ruddlesden-Popper <i>n</i> = 1, <i>n</i> = 2	~170 cm ⁻¹ (AgBr ₆) ⁵⁻ (BiBr ₆) ³⁻ octahedra symmetric stretching (A _g -like) ~140 cm ⁻¹ (AgBr ₆) ⁵⁻ (BiBr ₆) ³⁻ octahedra asymmetric stretching (E _g -like)	(PA) ₄ AgBiBr ₈ /(BA) ₄ AgBiBr ₈ /(PA) ₂ CsAgBiBr ₇ /(BA) ₂ CsAgBiBr ₇	Martín-García et al [77]
(BA) ₄ AgBiBr ₈			1100–1250 cm ⁻¹ C–N stretching	
(PEA) ₄ AgBiBr ₈			1250–1420 cm ⁻¹ CH ₂ twisting/wagging	
(PA) ₂ CsAgBiBr ₇			1420–1520 cm ⁻¹ CH ₂ bending	
(BA) ₂ CsAgBiBr ₇			1520–1650 cm ⁻¹ NH ₃ ⁺ bending and others	
(PEA) ₂ CsAgBiBr ₇			2850–2950 cm ⁻¹ CH ₂ stretching	
			2950–3100 cm ⁻¹ CH ₃ stretching	
		3100–3200 cm ⁻¹ NH ₃ ⁺ vibrations		
		(PEA) ₄ AgBiBr ₈ /(PEA) ₂ CsAgBiBr ₇		
		1100–1250 cm ⁻¹ C–N & C–C _{ring} stretching		
		1250–1420 cm ⁻¹ CH ₂ twisting/wagging		
		1420–1520 cm ⁻¹ CH ₂ bending		
		1520–1650 cm ⁻¹ NH ₃ ⁺ bending and others		
		2850–3050 cm ⁻¹ CH ₂ stretching		
		3050–3200 cm ⁻¹ CH aromatic vibrations		

^a Organic cations notation: MA = methylammonium; PA = formamidinium; GA = guanidinium; BA = butylammonium; HA = hexylammonium; NA = nonylammonium; UDA = undecylammonium; MDA = methyldecylammonium; MDDA = methyldodecylammonium; PEA = phenethylammonium; BzA = benzylammonium; EDDBE = 2,2-(ethylenedioxy)-bis(ethylammonium).



the phenyl rings results in a π - π stacking in the organic layer, providing more rigidity and larger volume, minimizing the possibility of an interlayer deformation [12, 77, 94, 109]. In a similar way, the halide anion plays a key role. The size of the perovskite lattice increases in accordance with the anionic radius series as $\text{Cl}^- < \text{Br}^- < \text{I}^-$. This translates into differences in the phase transition temperatures, as shown by Takahashi *et al* for Pb-based 2D HOIPs [110].

In this scenario, temperature-dependent Raman spectroscopy allows monitoring the dynamic order-disorder structural changes happening at the phase transition by studying the modes involving the R-NH_3^+ bonds and the inorganic octahedra vibrational modes. In this way, Moral *et al* [89] studied the phase transition of $(\text{BA})_2\text{PbI}_4$ prepared as powder and thin film. Their results demonstrated that R-NH_3^+ bonds behave as soft modes, i.e. modes whose energy goes to zero as the transition temperature is approached. The authors find that the temperature dependence of these soft modes is given by: $\omega(T) = \omega_0(T_0 - T)^{1/3}$, where T_0 is the transition temperature. The $1/3$ in the exponent corroborates that it is a second order transition with short-range correlations. Most interestingly, Moral *et al* highlight that the preparation method has an influence on the phase transition temperature, finding values of 230–242 K for powder and 260–278 K for thin films. Dragomir *et al* [87] also performed temperature-dependent Raman studies in $(\text{BA})_2\text{PbI}_4$ together with $(\text{PEA})_2\text{PbI}_4$, showing that the nature of the dynamic order-disorder transition is different. Using PEA, no first order phase transition exists in the range studied, while with BA there is a transition at 220–260 K. The relevance of the crystal structure is also highlighted. For example, the appearance of multiple modes in BA vs PEA can be due to the stiffening of the lattice due to octahedral distortion ($< 200 \text{ cm}^{-1}$). Moreover, some modes are more sensitive than others to the phase transition. In the case of the $(\text{BA})_2\text{PbI}_4$, due to the greater tilting of octahedra in the inorganic lattice, there is a high sensitivity of the Pb-I equatorial stretching vs Pb-I apical stretching mode to the phase transition. In $(\text{PEA})_2\text{PbI}_4$ an order-disorder transition at 100 K is evidenced by the broadening of organic-related vibrations and the suppression of others related to the π - π stacking among molecules. Going a step further in the Raman analysis of these materials, Menahem *et al* [79] used polarized-orientation Raman spectroscopy and compared the structural dynamics of MAPbI_3 with its layered counterparts, $(\text{BA})_2\text{PbI}_4$ and $(\text{PEA})_2\text{PbI}_4$

(figure 3(a)). In this way, they show that the structural dynamics of the layered counterparts has certain features in common with the 3D one. They exhibit similar Raman mode frequencies and atomic motions related to the inorganic lattice, which are split by the incorporation of the organic cations in the structure due to intermolecular interactions. Moreover, the authors gain insight into the order-disorder phase transition of $(\text{BA})_2\text{PbI}_4$ at ~ 274 K demonstrating that it involves the relaxation of octahedral tilting coupled to anharmonic thermal fluctuations, which affect the optoelectronic properties.

Apart from the temperature, another external stimulus than can promote structural changes and therefore, property modulation due the hybrid nature of the HOIPs, is pressure. Indeed, pressure up to 50 GPa has been applied to modulate the optoelectronic properties of these HOIPs. Recent studies have shown that the achievement of an effective bandgap tunability while keeping an efficient PL quantum yield is a matter of materials design, specifically, of properly selecting the organic cation in terms of molecule size and configuration. In 3D HOIPs PL tunability has been demonstrated for MAPbX_3 < 80 meV and for FAPbX_3 ~ 120 meV before PL quenching due to lattice distortion and bond bending. Instead, this tunability can be further increased using 2D HOIPs, reaching up to 520 meV, due to their layered nature and large A-site organic cations [69, 70]. Considering the sensibility of the vibrational properties to changes in the crystal structure and environment, Raman spectroscopy is a powerful tool to monitor these materials under pressure. In this way, Liu *et al* [69] determined an enhancement of the interlayer interaction of PEA cations as a systematic blueshift of the benzene ring mode during the hydrostatic compression applied to PEA_2PbI_4 microplates in a DAC. Furthermore, the Raman modes disappear at the same pressure as the PL quenching. This indicates that, when placed under pressure, the organic part is the first to be compressed (as it is softer). As pressure continues to increase, the inorganic lattice (harder part) begins to undergo changes as well, such as distortion and tilting. The process is irreversible and does not originate a phase transition. This is in contrast to the behaviour observed for $[(\text{BA})_2(\text{MA})_{n-1}\text{Pb}_n\text{I}_{3n+1}]$, $n = 1, 2, 3, 4$, which undergo phase transitions under compression, indicating the key role of the organic cation [111–113]. Indeed, a detailed recent *in-situ* Raman study in a DAC with single crystals by Yin *et al* [92] demonstrates that first the BA cation accommodates the compression by rotating along the C–C/C–N chain, leading to different consequences depending on the dimensionality of the HOIP. For $n = 1$, molecular tilting drives the adjacent inorganic layer to shift in the same direction, promoting a pressure-induced phase transition not observed for $n > 1$. Additionally, the $n = 1$ system presents an elastically reversible compressibility in terms of tilting and bond lengths, absent in the $n = 2$ case. All these changes were observed following the evolution of peak position and intensity of BA bending and rocking Raman modes under pressure (< 3.2 GPa) evidencing the rotation of the BA molecules during the compression. In detail, for $n = 2$, the bending (CCC) and (CCN) modes merge into one band accompanied by a decrease of the rocking modes' intensity and an enhancement of the Raman active modes related to the new BA conformers generated by the applied pressure. A further increase of the compression (> 5.5 GPa) all the BA-related Raman peaks become weak and disappear due to the structure amorphization [92]. For the $n = 1$ structure, the phase transitions ($\text{Pbca} \rightarrow \text{P2}_1/\text{a}$) were detected as a narrowing of the octahedral in-phase and out-of-phase bending modes in the low-frequency region of the Raman spectra with an additional octahedral out-of-phase rotation mode appearing in the $\text{P2}_1/\text{a}$ high-pressure phase. Moreover, the reorientation of the BA molecules is highlighted by the sharpening of the BA rocking mode in Pbca and the appearance of BA breathing and C–N stretching modes in the $\text{P2}_1/\text{a}$ phase. All these Raman shifts are reversible upon decompression [88]. In terms of pressure-induced PL modulation, $n = 1$ reaches ~ 300 meV, while $n = 2 \sim 190$ meV [88, 92]. Similarly, Guo *et al* [95] studied $(\text{HA})_2(\text{GA})\text{Pb}_2\text{I}_7$ crystals (HA = hexylammonium; GA = guanidinium) under pressure, observing a redshifted two-fold enhanced PL emission, with respect to the pristine material, which corresponds to a new phase, presenting even different colour. The monitoring of the Raman modes related to the Pb–I vibrations (~ 40 and ~ 110 cm^{-1}) allowed them to identify the lattice compression while increasing the pressure. Indeed, these modes systematically blueshift and sharpen in the new phase, but increasing the pressure leads to peaks broadening and weakening, revealing a higher structural disorder as result of the interlayer-distance reduction and lattice contraction. Most importantly, the changes introduced in the structure are irreversible, since the initial Raman spectrum and, therefore, the pristine crystal structure, are not recovered. Changing the halide, Li *et al* [70] studied the pressure effect on the PL emission of $[(\text{BA})_2(\text{MA})_{n-1}\text{Pb}_n\text{Br}_{3n+1}]$, $n = 1, 2$ crystals leading to redshifts of 520 meV for $n = 1$ and 230 meV for $n = 2$. Most importantly, the $(\text{BA})_2(\text{MA})\text{PbBr}_7$ ($n = 2$) crystal undergoes two different phase transitions, related to $(\text{PbBr}_6)^{4-}$ octahedra, BA, and MA molecule tilting motion, detected by the appearance of new octahedral motion-related Raman modes (figure 5(b)). In contrast, the BA_2PbBr_4 ($n = 1$) shows one phase transition, related to $(\text{PbBr}_6)^{4-}$ octahedra tilting and BA rearrangement, as indicated by the appearance of a Raman mode at ~ 30 cm^{-1} in the new phase, while inside the phase increasing the pressure systematically blueshifts and broadens the mode.

5. Electron-phonon interaction

Several important and interesting optical properties of 3D and 2D HOIPs arise from the strong and peculiar interaction of the charge carriers with the lattice vibrations, which are quite different from standard inorganic semiconductors [72]. Raman spectroscopy, as discussed above, is a valuable tool to obtain information about the typical energy and symmetry of the vibrational modes, and about the nature of lattice dynamics, such as anharmonicity and phonon lifetime, which are relevant in electron-phonon coupling.

As discussed in section 3, a peculiarity of vibrations in HOIPs is the large ion displacement due to the softness of the lattice, which results in anharmonic properties and localization of the phonon mode. Combined with the small effective mass of the electrons, the localization strongly affects the electron-phonon interaction, since it results in strong electric fields due to the ionic nature of the material. Because of this, the coupling of electrons and phonons cannot be neglected even in simpler descriptions of the material [72, 118]. This strong coupling is usually described in terms of polarons (i.e. a coupled state of excited electrons and ionic lattice deformation), but HOIPs have proved to need more detailed modelling. The polaron picture does not fully apply to HOIPs, and a better description considers the charges dynamically localized because of the slowly moving lattice, due to the anharmonic vibrations (dynamic disorder); this enables the prediction of properties such as the mobility and optical band gap [72, 119, 120].

Electron-phonon interaction is a critical mechanism in metal halide perovskite-based devices, as it intervenes in limiting the carrier mobility and the efficiency and broadening of the emission [121, 122]. Studies of PL dynamics have shown that polarons can form and interact with longitudinal optical phonons and that their large binding energy greatly affects the emission properties [123]. Furthermore, the photoexcited charges, while being mostly localized in the inorganic layers of the hybrid perovskite, can interact with vibrational modes of the inorganic part [124]. All these effects lead to broadband, white-light emission of interest for LEDs. Indeed, the polaronic effects are found to be very relevant for the fate of excited states in 2D HOIP, and several questions are open. For example, in 2D, free and self-trapped states could not coexist, as there is no energy barrier between the states. By contrast, in $\text{PEA}_2\text{PbCl}_4$ with $n = 1$, both emissions have been observed in PL, suggesting an interaction between the 2D layers [125].

The experimental techniques for assessing the electron-phonon coupling typically combine measurements of phonon spectra, such as Raman spectroscopy, with optical spectroscopy for the electronic transitions, such as PL and absorption. Time-resolved methods are especially useful, as they can identify the dynamics of the electronic transitions. Using PL, the effect of phonon modes stemming from the organic moieties has been found to affect the emission in more complex ways with respect to self-trapping or polaron confinement. In $(\text{BA})_2\text{PbI}_4$, Moral *et al* [89] found a double emission peak resulting from the splitting of the exciton by interaction with specific modes of the BA. Their picture of interaction is summarized in figure 6(a), as a subsequent relaxation of photoexcited hot electrons into free and then bound excitons, that are coupled by phonon emission. Here, Raman spectroscopy provides the necessary support to evaluate the energy of phonon modes (figure 6(b)), together with IR absorption. By comparing these results with the analysis of the PL linewidth, the authors identified the vibrational modes of the polar heads of BA as directly coupled with the exciton. A strong coupling between the vibrational modes of the inorganic cage and those of the organic part has also been reported [126]. This coupling can be mechanical, or can originate from electron-phonon interactions. Both cases would affect the dynamics of charges in the material.

Mauck *et al* [78] have used ultrafast time-resolved methods on thin films of $n = 1$ lead iodide with long alkyl chains $\text{C}_x\text{H}_{2x+1}\text{NH}_3^+$ with $x > 4$. Using femtosecond transient absorption, they photoexcited the material with a short resonant light pulse and probed the absorption as a function of time with a broadband light pulse. Since the pump pulse is shorter than the period of vibrations, the absorption is modulated by the motion of the atoms, and this is observed in the time domain as oscillations in the absorption, whose frequency corresponds to the energy of the vibrational modes coupled to the excited states. The Fourier transform of the oscillation (figure 2(b)), called the Resonant Impulsive-Stimulated Raman Spectra (RISRS), can then be compared directly to standard, continuous-wave Raman spectra. Mauck *et al* find that the energy of phonons coupled with the photoexcited states is in the range of the vibrations of the inorganic part, and varies little with the choice of organic moiety, in agreement with their study of PL linewidth. This is in contrast to the observations in short chain $(\text{BA})_2\text{PbI}_4$ ($x = 4$) [89], where the exciton dissociation was ascribed to interaction with organic modes.

Electron-phonon coupling is inherent to the Raman effect [57], yet in the typical measurement, when the excitation energy is far away from electronic resonances, the spectra are usually interpreted in a picture of independence of phonons and electrons. Instead, in resonant Raman the two systems are strongly coupled and their interaction is easily observed. Using this method, Gong *et al* [12] found differences in lead bromide with $n = 1$ for different type of cation, in particular BA and PEA. The resonant-excitation spectrum of the

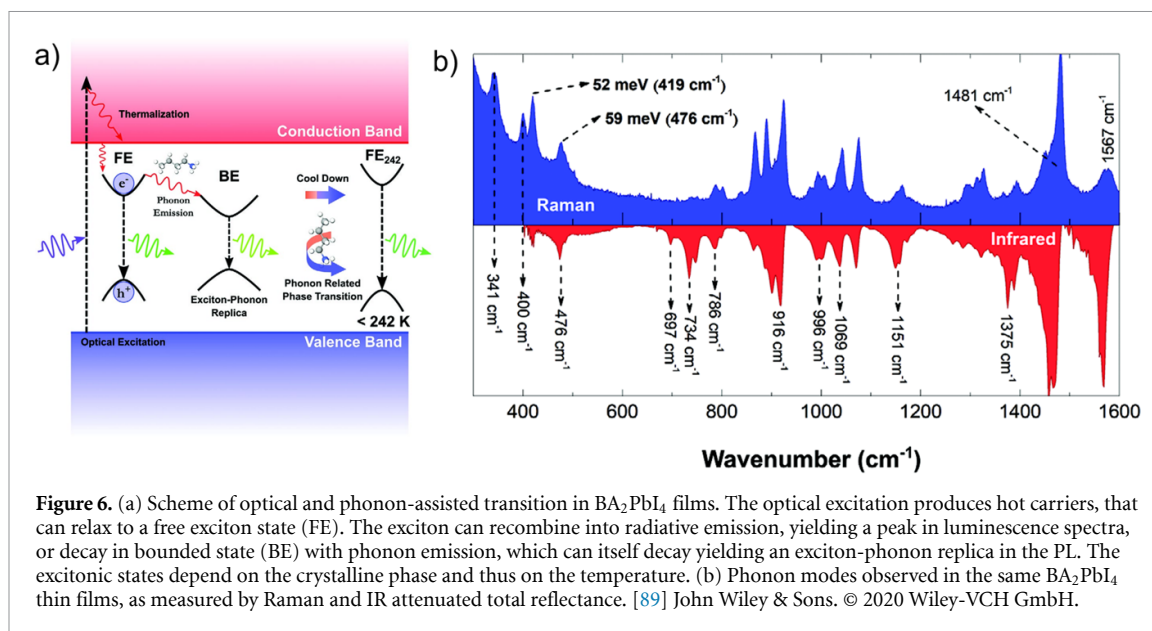


Figure 6. (a) Scheme of optical and phonon-assisted transition in BA_2PbI_4 films. The optical excitation produces hot carriers, that can relax to a free exciton state (FE). The exciton can recombine into radiative emission, yielding a peak in luminescence spectra, or decay in bounded state (BE) with phonon emission, which can itself decay yielding an exciton-phonon replica in the PL. The excitonic states depend on the crystalline phase and thus on the temperature. (b) Phonon modes observed in the same BA_2PbI_4 thin films, as measured by Raman and IR attenuated total reflectance. [89] John Wiley & Sons. © 2020 Wiley-VCH GmbH.

alkyl is much stronger than the one of the phenyl, indicating stronger electron-phonon coupling in the former system. This is associated with the lower rigidity of the alkyl chain. The effect of the stronger interaction in the alkyl sample is a larger non-radiative decay of photoexcited carriers, and thus a less efficient luminescence.

Another relevant peculiarity is the anharmonicity in the vibrational modes [46, 107, 127–130]; its effect on the electronic states must be taken into account, since thermal fluctuations, which are usually treated as a perturbation, can instead give rise to large deviations when the vibrations are not described by harmonic normal modes.

In the 3D case, especially in lead-iodides, these effects are very relevant, and are typically related to the small size of the cation that allows a tilting of the octahedra [131–133] away from high-symmetry configurations; in double perovskites such as $\text{Cs}_2\text{AgBiBr}_6$, which has been theoretically investigated by Klarbring *et al* [73], a soft and anharmonic lattice affects phase transitions and thermal conductivity. Recent results [46] have shown that in CsPbBr_3 and $\text{Cs}_2\text{AgBiBr}_6$ the anharmonicity has quite different effects, and these can be revealed by Raman spectroscopy. In the double perovskite, at high temperature, well-defined modes are observed, whose Raman activity and polarization dependence follow the prediction of group theory. In the single perovskite, the modes at high temperature are damped, and they break the predicted selection rules, indicating that the distortions associated with octahedral tilting (thus with the anharmonicity of the modes) is so strong that the equilibrium position of the ions is not described by the (average) cubic structures.

The case of layered perovskites in this respect needs to be investigated in more detail; it is expected that the movements of the octahedra can be large enough to bring the vibration beyond the harmonic approximation, due to the presence of large organic cation. Menahem *et al* [79] compared the case of 3D MAPbI_3 with 2D BA_2PbI_4 . At low temperature, the 2D HOIP has modes similar to the 3D, but they split because of the interaction with the organic moieties (or, correspondingly, because the crystal symmetry is reduced with respect to the 3D case, as discussed in the previous section). At high temperature, both crystals undergo a phase transition. From orthorhombic phase, MAPbI_3 becomes tetragonal at ~ 162 K. BA_2PbI_4 changes in another orthorhombic structure at ~ 274 K. In the high temperature phase, their Raman spectra exhibit broad features due to the strong anharmonic tilting. Similar to 3D MAPbI_3 , this is related to the phase transition via relaxational octahedral tilting, i.e. octahedral corrugation angles change, and there is an additional tilting due to the bonding between the iodides and the amine group.

As mentioned, electron-phonon coupling can be obtained by combining the Raman data and the optical properties of the crystals [12, 31, 134, 135]. Understanding a materials' electron-phonon coupling is essential for device design, as the coupling strength between the charge carriers and optical phonons plays a key role in determining the non-radiative recombination processes occurring in HOIP-based optoelectronic devices. The evaluation of the electron-phonon coupling from a quantitative point of view often relies on the Huang-Rhys factor (S) [136]. This factor can be calculated from the Stokes shift energy (ΔE_{Stokes}) [137] and the LO phonon energy ($\hbar\omega_{\text{LO}}$) of the strongest overtone as $\Delta E_{\text{Stokes}} = 2S\hbar\omega_{\text{LO}}$ [85, 134]. Another way to determine the Huang-Rhys factor is from the temperature dependent full width half maximum of the PL

signal using the equation: $FWHM = 2.36 \sqrt{S \hbar \omega_{\text{phonon}}} \sqrt{\cot\left(\frac{\hbar \omega_{\text{phonon}}}{2k_B T}\right)}$, where $\hbar \omega_{\text{phonon}}$ is the phonon energy [31]. Although the absolute S values obtained from both methods do not always match, the order of magnitude is similar, allowing to distinguish between strong ($S \gg 1$) and weak ($S \sim 1$) electron-phonon interaction. Estimations of the Huang-Rhys factor found in the literature usually show strong coupling for the 3D HOIPs, e.g. MAPbI₃ [138], Cs₂AgInCl₆ [31], Cs₂AgBiBr₆ [85, 134], or Cs₂Ag_{1-x}Na_xBiCl₆ ($0 < x < 1$) [139], while scarce values are reported for layered HOIPs [76, 77]. Thus, more efforts are needed in this direction to better exploit the 2D HOIPs for device integration.

6. Summary and perspective

We have presented the potential of Raman spectroscopy for the study of 2D HOIPs. The insight into the phonon modes provided by this technique is of great value to understand the optical and electronic properties of these hybrid materials. Methods such as polarization-dependent and resonant Raman spectroscopy can provide important information about the symmetry of the modes and their coupling with electrons and excitons. Temperature and pressure dependent measurements reveal an interesting landscape of phase transitions determining not only the temperature onset, but also their origin from a structural point of view. Additionally, this review highlights that the main focus has been done to date on Ruddlesden-Popper structures and Pb-based 2D HOIPs. These results will be important in the study of new compounds and crystal structures accessible when working with and designing 2D HOIPs, in combination with XRD measurements, by studying the coupling between organic cations- and inorganic lattice-related Raman modes. The effect of the localization of vibrations in the interaction with electrons and excitons can be explored, to assist in the challenge of incorporating layered HOIPs in devices such as solar cells with 2D/3D heterostructures. Here, Raman spectroscopy can be very useful to assess and monitor the quality of optoelectronic devices and their ambient stability. Finally, we mention that Raman spectroscopy has demonstrated to be a powerful tool to explore, locate and map the strain in layered materials and 3D HOIPs. However, until now this potential has only been investigated in early reports on 2D HOIPs. Furthermore, we envision that the versatility of Raman spectroscopy, with the possibility to couple with different set-ups, will play an important role in establishing the structure-properties relationship in layered HOIPs. This may be considered an essential first step towards the design and optimization of these hybrid materials for their use in high-performance optoelectronic devices.

Data availability statement

No new data were created or analysed in this study.

Acknowledgment

Authors thanks Dr E Goiri Little for reading and revising the manuscript.

Funding

This work is supported by the Spanish MCIN/AEI under Project PID2019-108153GA-I00, RTI2018-094861-B-I00 and under the María de Maeztu Units of Excellence Programme (MDM-2016-0618) & (Grant CEX2020-001038-M). B M-G thanks Gipuzkoa Council (Spain) in the frame of Gipuzkoa Fellows Program.

ORCID iDs

Davide Spirito  <https://orcid.org/0000-0002-6074-957X>

Yaiza Asensio  <https://orcid.org/0000-0001-5434-638X>

Luis E Hueso  <https://orcid.org/0000-0002-7918-8047>

Beatriz Martín-García  <https://orcid.org/0000-0001-7065-856X>

References

- [1] Kojima A, Teshima K, Shirai Y and Miyasaka T 2009 Organometal halide perovskites as visible-light sensitizers for photovoltaic cells *J. Am. Chem. Soc.* **131** 6050–1
- [2] NREL *Best Research-Cell Efficiency Chart* (available at: www.nrel.gov/pv/cell-efficiency.html) (Accessed 23 June 2022)
- [3] Grancini G and Nazeeruddin M K 2019 Dimensional tailoring of hybrid perovskites for photovoltaics *Nat. Rev. Mater.* **4** 4–22

- [4] Cheng X, Yang S, Cao B, Tao X and Chen Z 2020 Single crystal perovskite solar cells: development and perspectives *Adv. Funct. Mater.* **30** 1905021
- [5] Zhao B et al 2018 High-efficiency perovskite–polymer bulk heterostructure light-emitting diodes *Nat. Photon.* **12** 783–9
- [6] Miao J and Zhang F 2019 Recent progress on highly sensitive perovskite photodetectors *J. Mater. Chem. C* **7** 1741–91
- [7] Cao Y et al 2018 Perovskite light-emitting diodes based on spontaneously formed submicrometre-scale structures *Nature* **562** 249–53
- [8] Lin K et al 2018 Perovskite light-emitting diodes with external quantum efficiency exceeding 20 per cent *Nature* **562** 245–8
- [9] Boopathi K M et al 2020 Permanent lattice compression of lead-halide perovskite for persistently enhanced optoelectronic properties *ACS Energy Lett.* **5** 642–9
- [10] Ray A, Martín-García B, Martinelli A, Spirito D, Locardi F, Altamura D, Giannini C, Prato M, Manna L and Abdelhady A L 2020 Impact of local structure on halogen ion migration in layered methylammonium copper halide memory devices *J. Mater. Chem. A* **8** 17516–26
- [11] Ray A et al 2022 Mixed dimethylammonium/methylammonium lead halide perovskite single crystals for improved structural stability and enhanced photodetection *Adv. Mater.* **34** 2106160
- [12] Gong X et al 2018 Electron–phonon interaction in efficient perovskite blue emitters *Nat. Mater.* **17** 550–6
- [13] Saparov B and Mitzi D B 2016 Organic–inorganic perovskites: structural versatility for functional materials design *Chem. Rev.* **116** 4558–96
- [14] Tailor N K et al 2021 Advances in lead-free perovskite single crystals: fundamentals and applications *ACS Mater. Lett.* **3** 1025–80
- [15] Zhumekenov A A, Saidaminov M I, Mohammed O F and Bakr O M 2021 Stimuli-responsive switchable halide perovskites: taking advantage of instability *Joule* **5** 2027–46
- [16] Babayigit A, Ethirajan A, Muller M and Conings B 2016 Toxicity of organometal halide perovskite solar cells *Nat. Mater.* **15** 247–51
- [17] Ke W and Kanatzidis M G 2019 Prospects for low-toxicity lead-free perovskite solar cells *Nat. Commun.* **10** 965
- [18] Jena A K, Kulkarni A and Miyasaka T 2019 Halide perovskite photovoltaics: background, status, and future prospects *Chem. Rev.* **119** 3036–103
- [19] Yusoff A R B M and Nazeeruddin M K 2018 Low-dimensional perovskites: from synthesis to stability in perovskite solar cells *Adv. Energy Mater.* **8** 1702073
- [20] Berhe T A, Su W-N, Chen C-H, Pan C-J, Cheng J-H, Chen H-M, Tsai M-C, Chen L-Y, Dubale A A and Hwang B-J 2016 Organometal halide perovskite solar cells: degradation and stability *Energy Environ. Sci.* **9** 323–56
- [21] Du Y et al 2021 Electric-field-induced ion migration behavior in methylammonium lead iodide perovskite *J. Phys. Chem. Lett.* **12** 7106–12
- [22] Li C, Guerrero A, Zhong Y, Gräser A, Luna C A M, Köhler J, Bisquert J, Hildner R and Huettnner S 2017 Real-time observation of iodide ion migration in methylammonium lead halide perovskites *Small* **13** 1701711
- [23] Dong Q, Lei L, Mendes J and So F 2020 Operational stability of perovskite light emitting diodes *J. Phys. Mater.* **3** 012002
- [24] Connor B A, Leppert L, Smith M D, Neaton J B and Karunadasa H I 2018 Layered halide double perovskites: dimensional reduction of Cs₂AgBiBr₆ *J. Am. Chem. Soc.* **140** 5235–40
- [25] Shao S, Liu J, Portale G, H-f F, Blake G R, G H T B, Koster L J A and Loi M A 2018 Highly reproducible Sn-based hybrid perovskite solar cells with 9% efficiency *Adv. Energy Mater.* **8** 1702019
- [26] Pantaler M, Cho K T, Queloz V I E, García Benito I, Fettkenhauer C, Anusca I, Nazeeruddin M K, Lupascu D C and Grancini G 2018 Hysteresis-free lead-free double-perovskite solar cells by interface engineering *ACS Energy Lett.* **3** 1781–6
- [27] De Angelis F 2021 The prospect of lead-free perovskite photovoltaics *ACS Energy Lett.* **6** 1586–7
- [28] Pitaro M, Tekelenburg E K, Shao S and Loi M A 2022 Tin halide perovskites: from fundamental properties to solar cells *Adv. Mater.* **34** 2105844
- [29] Xiao Z, Song Z and Yan Y 2019 From lead halide perovskites to lead-free metal halide perovskites and perovskite derivatives *Adv. Mater.* **31** 1803792
- [30] Vargas B, Rodríguez-López G and Solís-Ibarra D 2020 The emergence of halide layered double perovskites *ACS Energy Lett.* **5** 3591–608
- [31] Luo J et al 2018 Efficient and stable emission of warm-white light from lead-free halide double perovskites *Nature* **563** 541–5
- [32] Palumbo M, Berrios E, Varsano D and Giorgi G 2020 Optical properties of lead-free double perovskites by *ab initio* excited-state methods *ACS Energy Lett.* **5** 457–63
- [33] Mir S A and Gupta D C 2020 Analysis of cage structured halide double perovskites Cs₂NaMCl₆ (M = Ti, V) by spin polarized calculations *J. Alloys Compd.* **854** 156000
- [34] Buizza L R V, Sansom H C, Wright A D, Ulatowski A M, Johnston M B, Snaith H J and Herz L M 2022 Interplay of structure, charge-carrier localization and dynamics in copper-silver-bismuth-halide semiconductors *Adv. Funct. Mater.* **32** 2108392
- [35] Leng K, Fu W, Liu Y, Chhowalla M and Loh K P 2020 From bulk to molecularly thin hybrid perovskites *Nat. Rev. Mater.* **5** 482–500
- [36] Smith M D, Connor B A and Karunadasa H I 2019 Tuning the luminescence of layered halide perovskites *Chem. Rev.* **119** 3104–39
- [37] Li X, Hoffman J M and Kanatzidis M G 2021 The 2D halide perovskite rulebook: how the spacer influences everything from the structure to optoelectronic device efficiency *Chem. Rev.* **121** 2230–91
- [38] Fang C, Wang H and Li D 2021 Recent progress in two-dimensional Ruddlesden–Popper perovskite based heterostructures *2D Mater.* **8** 022006
- [39] Ricciardulli A G, Yang S, Smet J H and Saliba M 2021 Emerging perovskite monolayers *Nat. Mater.* **20** 1325–36
- [40] Mao L, Stoumpos C C and Kanatzidis M G 2019 Two-dimensional hybrid halide perovskites: principles and promises *J. Am. Chem. Soc.* **141** 1171–90
- [41] Xing J et al 2018 Color-stable highly luminescent sky-blue perovskite light-emitting diodes *Nat. Commun.* **9** 3541
- [42] Wang H, Li S, Liu X, Shi Z, Fang X and He J 2021 Low-dimensional metal halide Perovskite photodetectors *Adv. Mater.* **33** 2003309
- [43] Leguy A M A et al 2016 Dynamic disorder, phonon lifetimes, and the assignment of modes to the vibrational spectra of methylammonium lead halide perovskites *Phys. Chem. Chem. Phys.* **18** 27051–66
- [44] Yin T, Fang Y, Fan X, Zhang B, Kuo J-L, White T J, Chow G M, Yan J and Shen Z X 2017 Hydrogen-bonding evolution during the polymorphic transformations in CH₃NH₃PbBr₃: experiment and theory *Chem. Mater.* **29** 5974–81
- [45] Maćzka M, Ptak M, Vasconcelos D L M, Giriunas L, Freire P T C, Bertmer M, Banys J and Simenas M 2020 NMR and Raman scattering studies of temperature- and pressure-driven phase transitions in CH₃NH₂NH₂PbCl₃ perovskite *J. Phys. Chem. C* **124** 26999–7008

- [46] Cohen A, Brenner T M, Klarbring J, Sharma R, Fabini D H, Korobko R, Nayak P K, Hellman O and Yaffe O 2022 Diverging expressions of anharmonicity in halide perovskites *Adv. Mater.* **34** 2107932
- [47] Talit K and Strubbe D A 2020 Stress effects on vibrational spectra of a cubic hybrid perovskite: a probe of local strain *J. Phys. Chem. C* **124** 27287–99
- [48] Ledinský M, Löper P, Niesen B, Holovský J, Moon S-J, Yum J-H, De Wolf S, Fejfar A and Ballif C 2015 Raman spectroscopy of organic–inorganic halide perovskites *J. Phys. Chem. Lett.* **6** 401–6
- [49] Hooper K E A, Lee H K H, Newman M J, Meroni S, Baker J, Watson T M and Tsoi W C 2017 Probing the degradation and homogeneity of embedded perovskite semiconducting layers in photovoltaic devices by Raman spectroscopy *Phys. Chem. Chem. Phys.* **19** 5246–53
- [50] Pistor P, Ruiz A, Cabot A and Izquierdo-Roca V 2016 Advanced Raman spectroscopy of methylammonium lead iodide: development of a non-destructive characterisation methodology *Sci. Rep.* **6** 35973
- [51] Liao M, Shan B and Li M 2019 *In situ* Raman spectroscopic studies of thermal stability of all-inorganic cesium lead halide (CsPbX₃, X=Cl, Br, I) perovskite nanocrystals *J. Phys. Chem. Lett.* **10** 1217–25
- [52] Ibaceta-Jaña J et al 2020 Vibrational dynamics in lead halide hybrid perovskites investigated by Raman spectroscopy *Phys. Chem. Chem. Phys.* **22** 5604–14
- [53] Debnath T, Sarker D, Huang H, Han Z-K, Dey A, Polavarapu L, Levchenko S V and Feldmann J 2021 Coherent vibrational dynamics reveals lattice anharmonicity in organic–inorganic halide perovskite nanocrystals *Nat. Commun.* **12** 2629
- [54] Ruan S, McMeekin D P, Fan R, Webster N A S, Ebendorff-Heidepriem H, Cheng Y-B, Lu J, Ruan Y and McNeill C R 2020 Raman spectroscopy of formamidinium-based lead halide perovskite single crystals *J. Phys. Chem. C* **124** 2265–72
- [55] Grancini G et al 2014 The impact of the crystallization processes on the structural and optical properties of hybrid perovskite films for photovoltaics *J. Phys. Chem. Lett.* **5** 3836–42
- [56] Satta J, Melis C, Carbonaro C M, Pinna A, Salado M, Salazar D and Ricci P C 2021 Raman spectra and vibrational analysis of CsPbI₃: a fast and reliable technique to identify lead halide perovskite polymorphs *J. Mater. Chem. C* **7** 127–35
- [57] Yu P Y and Cardona M 2010 Optical Properties II *Fundamentals of Semiconductors* Graduate Texts in Physics (Berlin: Springer) pp 345–426
- [58] Glebov A L, Mokhun O, Rapaport A, Vergnole S, Smirnov V and Glebov L B 2012 Volume Bragg gratings as ultra-narrow and multiband optical filters *Proc. SPIE* **8428** 84280C
- [59] Tan P H et al 2012 The shear mode of multilayer graphene *Nat. Mater.* **11** 294–300
- [60] Aroyo M I, Perez-Mato J M, Capillas C, Kroumova E, Ivantchev S, Madariaga G, Kirov A and Wondratschek H 2006 Bilbao crystallographic server: I. Databases and crystallographic computing programs *Z. Für Krist.—Cryst. Mater.* **221** 15–27
- [61] Giustino F and Snaith H J 2016 Toward lead-free perovskite solar cells *ACS Energy Lett.* **1** 1233–40
- [62] Nakamoto K 2008 *Infrared and Raman Spectra of Inorganic and Coordination Compounds* (Hoboken, NJ: Wiley)
- [63] Krumova E, Aroyo M I, Perez-Mato J M, Kirov A, Capillas C, Ivantchev S and Wondratschek H 2003 Bilbao Crystallographic Server: useful databases and tools for phase transitions studies *Phase Transit.* **76** 155–70
- [64] Cong X, Liu X-L, Lin M-L and Tan P-H 2020 Application of Raman spectroscopy to probe fundamental properties of two-dimensional materials *npj 2D Mater. Appl.* **4** 13
- [65] Lin M-L, Leng Y-C, Cong X, Meng D, Wang J, Li X-L, Yu B, Liu X-L, Yu X-F and Tan P-H 2020 Understanding angle-resolved polarized Raman scattering from black phosphorus at normal and oblique laser incidences *Sci. Bull.* **65** 1894–900
- [66] Kim J, Lee J-U and Cheong H 2020 Polarized Raman spectroscopy for studying two-dimensional materials *J. Phys.: Condens. Matter* **32** 343001
- [67] Liu X-L, Zhang X, Lin M-L and Tan P-H 2017 Different angle-resolved polarization configurations of Raman spectroscopy: a case on the basal and edge plane of two-dimensional materials *Chin. Phys. B* **26** 067802
- [68] Azeem M, Qin Y, Li Z-G and Li W 2021 Cooperative B-site octahedral tilting, distortion and A-site conformational change induced phase transitions of a 2D lead halide perovskite *Mater. Chem. Front.* **5** 7587–94
- [69] Liu S et al 2019 Manipulating efficient light emission in two-dimensional perovskite crystals by pressure-induced anisotropic deformation *Sci. Adv.* **5** eaav9445
- [70] Li H, Qin Y, Shan B, Shen Y, Ersan F, Soignard E, Ataca C and Tongay S 2020 Unusual pressure-driven phase transformation and band renormalization in 2D vdW hybrid lead halide perovskites *Adv. Mater.* **32** 1907364
- [71] Schrader B 1973 Chemical applications of Raman spectroscopy *Angew. Chem., Int. Ed. Engl.* **12** 884–908
- [72] Schilcher M J, Robinson P J, Abramovitch D J, Tan L Z, Rappe A M, Reichman D R and Egger D A 2021 The significance of polarons and dynamic disorder in halide perovskites *ACS Energy Lett.* **6** 2162–73
- [73] Klarbring J, Hellman O, Abrikosov I A and Simak S I 2020 Anharmonicity and ultralow thermal conductivity in lead-free halide double perovskites *Phys. Rev. Lett.* **125** 045701
- [74] Gehrman C and Egger D A 2019 Dynamic shortening of disorder potentials in anharmonic halide perovskites *Nat. Commun.* **10** 3141
- [75] Sharma R, Dai Z, Gao L, Brenner T M, Yadgarov L, Zhang J, Rakita Y, Korobko R, Rappe A M and Yaffe O 2020 Elucidating the atomistic origin of anharmonicity in tetragonal CH₃NH₃PbI₃ with Raman scattering *Phys. Rev. Mater.* **4** 092401
- [76] Lin M-L, Dhanabalan B, Biffi G, Leng Y-C, Kutkan S, Arciniégas M P, Tan P-H and Krahn R 2022 Correlating symmetries of low-frequency vibrations and self-trapped excitons in layered perovskites for light emission with different colours *Small* **18** 2106759
- [77] Martín-García B, Spirito D, Biffi G, Artyukhin S, Bonaccorso F and Krahn R 2021 Phase transitions in low-dimensional layered double perovskites: the role of the organic moieties *J. Phys. Chem. Lett.* **12** 280–6
- [78] Mauck C M, France-Lanord A, Hernandez O A C, Dahod N S, Grossman J C and Tisdale W A 2019 Inorganic cage motion dominates excited-state dynamics in 2D-layered perovskites (C_xH_{2x+1}NH₃)₂PbI₄ (x = 4–9) *J. Phys. Chem. C* **123** 27904–16
- [79] Menahem M, Dai Z, Aharon S, Sharma R, Asher M, Diskin-Posner Y, Korobko R, Rappe A M and Yaffe O 2021 Strongly anharmonic octahedral tilting in two-dimensional hybrid halide perovskites *ACS Nano* **15** 10153–62
- [80] Quarti C, Grancini G, Mosconi E, Bruno P, Ball J M, Lee M M, Snaith H J, Petrozza A and Angelis F D 2014 The Raman spectrum of the CH₃NH₃PbI₃ hybrid perovskite: interplay of theory and experiment *J. Phys. Chem. Lett.* **5** 279–84
- [81] Francisco-López A, Charles B, Weber O J, Alonso M I, Garriga M, Campoy-Quiles M, Weller M T and Goñi A R 2018 Pressure-induced locking of methylammonium cations versus amorphization in hybrid lead iodide perovskites *J. Phys. Chem. C* **122** 22073–82

- [82] Pérez-Osorio M A, Lin Q, Phillips R T, Milot R L, Herz L M, Johnston M B and Giustino F 2018 Raman spectrum of the organic–inorganic halide perovskite $\text{CH}_3\text{NH}_3\text{PbI}_3$ from first principles and high-resolution low-temperature Raman measurements *J. Phys. Chem. C* **122** 21703–17
- [83] Sharma R et al 2020 Lattice mode symmetry analysis of the orthorhombic phase of methylammonium lead iodide using polarized Raman *Phys. Rev. Mater.* **4** 051601
- [84] Guo Y, Yaffe O, Paley D W, Beecher A N, Hull T D, Szpak G, Owen J S, Brus L E and Pimenta M A 2017 Interplay between organic cations and inorganic framework and incommensurability in hybrid lead-halide perovskite $\text{CH}_3\text{NH}_3\text{PbBr}_3$ *Phys. Rev. Mater.* **1** 042401
- [85] Zelewski S J et al 2019 Revealing the nature of photoluminescence emission in the metal-halide double perovskite $\text{Cs}_2\text{AgBiBr}_6$ *J. Mater. Chem. C* **7** 8350–6
- [86] Cortecchia D, Neutzner S, Srimath Kandada A R, Mosconi E, Meggiolaro D, De Angelis F, Soci C and Petrozza A 2017 Broadband emission in two-dimensional hybrid perovskites: the role of structural deformation *J. Am. Chem. Soc.* **139** 39–42
- [87] Dragomir V A, Neutzner S, Quarti C, Cortecchia D, Petrozza A, Roorda S, Beljonne D, Leonelli R, Kandada A R S and Silva C 2018 Lattice vibrations and dynamic disorder in two-dimensional hybrid lead-halide perovskites (arXiv:181205255 [Cond-Mat Physicsphysics])
- [88] Yin T et al 2019 Pressure-engineered structural and optical properties of two-dimensional $(\text{C}_4\text{H}_9\text{NH}_3)_2\text{PbI}_4$ perovskite exfoliated nm-thin flakes *J. Am. Chem. Soc.* **141** 1235–41
- [89] Moral R F, Germino J C, Bonato L G, Almeida D B, Therézio E M, Atvars T D Z, Stranks S D, Nome R A and Nogueira A F 2020 Influence of the vibrational modes from the organic moieties in 2D lead halides on excitonic recombination and phase transition *Adv. Opt. Mater.* **8** 2001431
- [90] Dahod N S, France-Lanord A, Paritmongkol W, Grossman J C and Tisdale W A 2020 Low-frequency Raman spectrum of 2D layered perovskites: local atomistic motion or superlattice modes? *J. Chem. Phys.* **153** 044710
- [91] Lavan S N, Sanni A M, Rury A S and Liu Z-F 2021 Characterization of the ammonium bending vibrations in two-dimensional hybrid lead-halide perovskites from Raman spectroscopy and first-principles calculations *J. Phys. Chem. C* **125** 223–36
- [92] Yin T et al 2022 Pressure driven rotational isomerism in 2D hybrid perovskites *Research Square* (<https://doi.org/10.21203/rs.3.rs-1394948/v1>) (Accessed 10 March 2022)
- [93] Abid H, Trigui A, Mlayah A, Hlil E K and Abid Y 2012 Phase transition in organic–inorganic perovskite $(\text{C}_9\text{H}_{19}\text{NH}_3)_2\text{PbI}_2\text{Br}_2$ of long-chain alkylammonium *Results Phys.* **2** 71–76
- [94] Dhanabalan B, Leng Y-C, Biffi G, Lin M-L, Tan P-H, Infante I, Manna L, Arciniegas M P and Krahn R 2020 Directional anisotropy of the vibrational modes in 2D-layered perovskites *ACS Nano* **14** 4689–97
- [95] Guo S et al 2020 Pressure-suppressed carrier trapping leads to enhanced emission in two-dimensional perovskite $(\text{HA})_2(\text{GA})\text{Pb}_2\text{I}_7$ *Angew. Chem., Int. Ed.* **59** 17533–9
- [96] Selivanov N I et al 2021 Hybrid organic–inorganic halide post-perovskite 3-Cyanopyridinium lead tribromide for optoelectronic applications *Adv. Funct. Mater.* **31** 2102338
- [97] Yaffe O et al 2017 Local polar fluctuations in lead halide perovskite crystals *Phys. Rev. Lett.* **118** 136001
- [98] Robinson K, Gibbs G V and Ribbe P H 1971 Quadratic elongation: a quantitative measure of distortion in coordination polyhedra *Science* **172** 567–70
- [99] Bartels R A, Oron D and Rigneault H 2021 Low frequency coherent Raman spectroscopy *J. Phys. Photonics* **3** 042004
- [100] Girard A, Saviot L, Pedetti S, Tessier M D, Margueritat J, Gehan H, Mahler B, Dubertret B and Mermet A 2016 The mass load effect on the resonant acoustic frequencies of colloidal semiconductor nanoplatelets *Nanoscale* **8** 13251–6
- [101] Lee E M Y, Mork A J, Willard A P and Tisdale W A 2017 Including surface ligand effects in continuum elastic models of nanocrystal vibrations *J. Chem. Phys.* **147** 044711
- [102] Lin M-L, Miscuglio M, Polovitsyn A, Leng Y-C, Martín-García B, Moreels I, Tan P-H and Krahn R 2019 Giant-shell CdSe/CdS nanocrystals: exciton coupling to shell phonons investigated by resonant Raman spectroscopy *J. Phys. Chem. Lett.* **10** 399–405
- [103] Miscuglio M, Lin M-L, Di Stasio F, Tan P-H and Krahn R 2016 Confined acoustic phonons in colloidal nanorod heterostructures investigated by nonresonant Raman spectroscopy and finite elements simulations *Nano Lett.* **16** 7664–70
- [104] Sapriel J and Rouhani B D 1989 Vibrations in superlattices *Surf. Sci. Rep.* **10** 189–275
- [105] Bechtel J S, Thomas J C and Van der Ven A 2019 Finite-temperature simulation of anharmonicity and octahedral tilting transitions in halide perovskites *Phys. Rev. Mater.* **3** 113605
- [106] Lin C-W et al 2020 Structure-dependent photoluminescence in low-dimensional ethylammonium, propylammonium, and butylammonium lead iodide perovskites *ACS Appl. Mater. Interfaces* **12** 5008–16
- [107] Gélvez-Rueda M C, Hutter E M, Cao D H, Renaud N, Stoumpos C C, Hupp J T, Savenije T J, Kanatzidis M G and Grozema F C 2017 Interconversion between free charges and bound excitons in 2D hybrid lead halide perovskites *J. Phys. Chem. C* **121** 26566–74
- [108] Billing D G and Lemmerer A 2007 Synthesis, characterization and phase transitions in the inorganic-organic layered perovskite-type hybrids $[(\text{C}_n\text{H}_{2n} + 1\text{NH}_3)_2\text{PbI}_4]$, $n = 4, 5$ and 6 *Acta Crystallogr. B* **63** 735–47
- [109] Tu Q, Spanopoulos I, Vasileiadou E S, Li X, Kanatzidis M G, Shekhawat G S and Dravid V P 2020 Exploring the factors affecting the mechanical properties of 2D hybrid organic–inorganic perovskites *ACS Appl. Mater. Interfaces* **12** 20440–7
- [110] Takahashi M, Hoshino N, Sambe K, Takeda T and Akutagawa T 2020 Dynamics of chiral cations in two-dimensional CuX_4 and PbX_4 perovskites ($X = \text{Cl}$ and Br) *Inorg. Chem.* **59** 11606–15
- [111] Liu G et al 2017 Two regimes of bandgap red shift and partial ambient retention in pressure-treated two-dimensional perovskites *ACS Energy Lett.* **2** 2518–24
- [112] Liu G et al 2018 Isothermal pressure-derived metastable states in 2D hybrid perovskites showing enduring bandgap narrowing *Proc. Natl Acad. Sci.* **115** 8076–81
- [113] Feng G, Qin Y, Ran C, Ji L, Dong L and Li W 2018 Structural evolution and photoluminescence properties of a 2D hybrid perovskite under pressure *APL Mater.* **6** 114201
- [114] Momma K and Izumi F 2011 VESTA 3 for three-dimensional visualization of crystal, volumetric and morphology data *J. Appl. Crystallogr.* **44** 1272–6
- [115] Schade L et al 2019 Structural and optical properties of $\text{Cs}_2\text{AgBiBr}_6$ double perovskite *ACS Energy Lett.* **4** 299–305
- [116] Smith M D, Jaffe A, Dohner E R, Lindenberg A M and Karunadasa H I 2017 Structural origins of broadband emission from layered Pb–Br hybrid perovskites *Chem. Sci.* **8** 4497–504
- [117] Li L, Liu X, Li Y, Xu Z, Wu Z, Han S, Tao K, Hong M, Luo J and Sun Z 2019 Two-dimensional hybrid perovskite-type ferroelectric for highly polarization-sensitive shortwave photodetection *J. Am. Chem. Soc.* **141** 2623–9

- [118] Blancon J-C, Even J, Stoumpos C C, Kanatzidis M G and Mohite A D 2020 Semiconductor physics of organic–inorganic 2D halide perovskites *Nat. Nanotechnol.* **15** 969–85
- [119] Mayers M Z, Tan L Z, Egger D A, Rappe A M and Reichman D R 2018 How lattice and charge fluctuations control carrier dynamics in halide perovskites *Nano Lett.* **18** 8041–6
- [120] Lacroix A, de Laissardière G T, Quémerais P, Julien J-P and Mayou D 2020 Modeling of electronic mobilities in halide perovskites: adiabatic quantum localization scenario *Phys. Rev. Lett.* **124** 196601
- [121] Righetto M, Giovanni D, Lim S S and Sum T C 2021 The photophysics of Ruddlesden–Popper perovskites: a tale of energy, charges, and spins *Appl. Phys. Rev.* **8** 011318
- [122] Chen Y, Sun Y, Peng J, Tang J, Zheng K and Liang Z 2018 2D Ruddlesden–Popper perovskites for optoelectronics *Adv. Mater.* **30** 1703487
- [123] Guo Z, Wu X, Zhu T, Zhu X and Huang L 2016 Electron–phonon scattering in atomically thin 2D perovskites *ACS Nano* **10** 9992–8
- [124] Straus D B, Hurtado Parra S, Iotov N, Gebhardt J, Rappe A M, Subotnik J E, Kikkawa J M and Kagan C R 2016 Direct observation of electron–phonon coupling and slow vibrational relaxation in organic–inorganic hybrid perovskites *J. Am. Chem. Soc.* **138** 13798–801
- [125] Thirumal K et al 2017 Morphology-independent stable white-light emission from self-assembled two-dimensional perovskites driven by strong exciton–phonon coupling to the organic framework *Chem. Mater.* **29** 3947–53
- [126] Grechko M, Bretschneider S A, Vietze L, Kim H and Bonn M 2018 Vibrational coupling between organic and inorganic sublattices of hybrid perovskites *Angew. Chem., Int. Ed.* **57** 13657–61
- [127] Traore B et al 2018 Composite nature of layered hybrid perovskites: assessment on quantum and dielectric confinements and band alignment *ACS Nano* **12** 3321–32
- [128] Mauck C M and Tisdale W A 2019 Excitons in 2D organic–inorganic halide perovskites *Trends Chem.* **1** 380–93
- [129] Srimath Kandada A R and Silva C 2020 Exciton polarons in two-dimensional hybrid metal-halide perovskites *J. Phys. Chem. Lett.* **11** 3173–84
- [130] Yin J, Li H, Cortecchia D, Soci C and Brédas J-L 2017 Excitonic and polaronic properties of 2D hybrid organic–inorganic perovskites *ACS Energy Lett.* **2** 417–23
- [131] Bertolotti F, Protesescu L, Kovalenko M V, Yakunin S, Cervellino A, Billinge S J L, Terban M W, Pedersen J S, Masciocchi N and Guagliardi A 2017 Coherent nanotwins and dynamic disorder in cesium lead halide perovskite nanocrystals *ACS Nano* **11** 3819–31
- [132] Beecher A N, Semonin O E, Skelton J M, Frost J M, Terban M W, Zhai H, Alatas A, Owen J S, Walsh A and Billinge S J L 2016 Direct observation of dynamic symmetry breaking above room temperature in methylammonium lead iodide perovskite *ACS Energy Lett.* **1** 880–7
- [133] Cottingham P and Brutchey R L 2018 Depressed phase transitions and thermally persistent local distortions in CsPbBr₃ quantum dots *Chem. Mater.* **30** 6711–6
- [134] Steele J A et al 2018 Giant electron–phonon coupling and deep conduction band resonance in metal halide double perovskite *ACS Nano* **12** 8081–90
- [135] Wang Z-W, Sun Y, Cui Y, Xiao Y, Deng J-P, Xiong W and Li Z-Q 2021 Quantum defect-assisted multiphonon Raman scattering in metal halide perovskites *J. Phys.: Condens. Matter* **33** 145702
- [136] Huang K and Rhys A 1950 Theory of light absorption and non-radiative transitions in *F*-centres *Proc. R. Soc. A* **204** 406–23
- [137] de Jong M, Seijo L, Meijerink A and Rabouw F T 2015 Resolving the ambiguity in the relation between Stokes shift and Huang–Rhys parameter *Phys. Chem. Chem. Phys.* **17** 16959–69
- [138] Whalley L D, van Gerwen P, Frost J M, Kim S, Hood S N and Walsh A 2021 Giant Huang–Rhys factor for electron capture by the iodine interstitial in perovskite solar cells *J. Am. Chem. Soc.* **143** 9123–8
- [139] Dakshinamurthy A C and Sudakar C 2022 Sublattice distortion enabled strong interplay between phonon vibrations, electron–phonon coupling, and self-trapped excitonic emissions in Cs₂Ag_{1-x}Na_xBiCl₆ double perovskites *J. Phys. Chem. Lett.* **13** 433–9